



Originally published as:

Krüger, F., Dahm, T., Hannemann, K. (2020): Mapping of Eastern North Atlantic Ocean seismicity from Po/So observations at a mid-aperture seismological broad-band deep sea array. - *Geophysical Journal International*, 221, 2, 1055-1080.

<https://doi.org/10.1093/gji/ggaa054>

Mapping of Eastern North Atlantic Ocean seismicity from *Po/So* observations at a mid-aperture seismological broad-band deep sea array

Frank Krüger,¹ Torsten Dahm^{1,2} and Katrin Hannemann³

¹*Institute of Geosciences, University of Potsdam, Potsdam, Germany. E-mail: kruegerf@geo.uni-potsdam.de*

²*Section 2.1, Physics of Earthquakes and Volcanoes, Helmholtz Centre Potsdam, GFZ German Research Centre for Geosciences, Potsdam, Germany*

³*Institute for Geophysics and Geology, University of Leipzig, Leipzig, Germany*

Accepted 2020 January 28. Received 2020 January 28; in original form 2019 August 21

SUMMARY

A mid-aperture broad-band test array (OBS array DOCTAR) was deployed from June 2011 to April 2012 about 100 km north of the Gloria fault in the Eastern North Atlantic in about 5000 m water depth. In addition arrays were installed on Madeira Island and in western Portugal mainland. For the first time in the Eastern North Atlantic, we recorded a large number of high frequency *Po* and *So* waves from local and regional small and moderate earthquakes ($M_L < 4$). An incoherent beamforming method was adapted to scan continuous data for such *Po* and *So* arrivals applying a sliding window waveform migration and frequency–wavenumber technique. We identify about 320 *Po* and 1550 *So* arrivals and compare the phase onsets with the ISC catalogue (ISC 2015) for the same time span. Up to a distance of 6° to the DOCTAR stations all events listed in the ISC catalogue could be associated to *Po* and *So* phases. Arrivals from events in more than 10° distance could be identified only in some cases. Only few *Po* and/or *So* arrivals were detected for earthquakes from the European and African continental area, the continental shelf regions and for earthquakes within or northwest of the Azores plateau. Unexpectedly, earthquake clusters are detected within the oceanic plates north and south of the Gloria fault and far from plate boundaries, indicating active intraplate structures. We also observe and locate numerous small magnitude earthquakes on the segment of the Gloria fault directly south of DOCTAR, which likely coincides with the rupture of the 25 November 1941 event. Local small magnitude earthquakes located beneath DOCTAR show hypocentres up to 30 km depth and strike-slip focal mechanisms. A comparison with detections at temporary mid-aperture arrays on Madeira and in western Portugal shows that the deep ocean array performs much better than the island and the continental array regarding the detection threshold for events in the oceanic plates.

We conclude that sparsely distributed mid-aperture seismic arrays in the deep ocean could decrease the detection and location threshold for seismicity with $M_L < 4$ in the oceanic plate and might constitute a valuable tool to monitor oceanic plate seismicity.

Key words: Body waves; Earthquake source observations; Seismicity and tectonics.

1 INTRODUCTION

The DOCTAR (Deep Ocean Test ARray) experiment was planned to study the oceanic lithosphere and upper mantle by array seismological means and to investigate the monitoring performance of a deep sea seismological array in comparison to standard seismological array setups in a continental region and on an oceanic island. The project was organized by geophysics groups from University of Potsdam, University of Hamburg and the Instituto dom Luis (IDL) in Portugal. In the framework of this project, three arrays were

installed, one in the deep sea west of Portugal in the eastern Atlantic (water depth of about 5000 m, hereafter referred to as DOCTAR), a second one on the island of Madeira and a third one in western Portugal mainland near the city of Evora (Fig. 1). DOCTAR was deployed in June 2011 and recovered in April 2012. The Madeira array and the Evora array were operating slightly longer from May 2011 to October 2012. DOCTAR and the array in Portugal mainland are of similar size with an overall aperture of about 70 km, while the Madeira Island array had an aperture of only 30 km (Fig. 1)

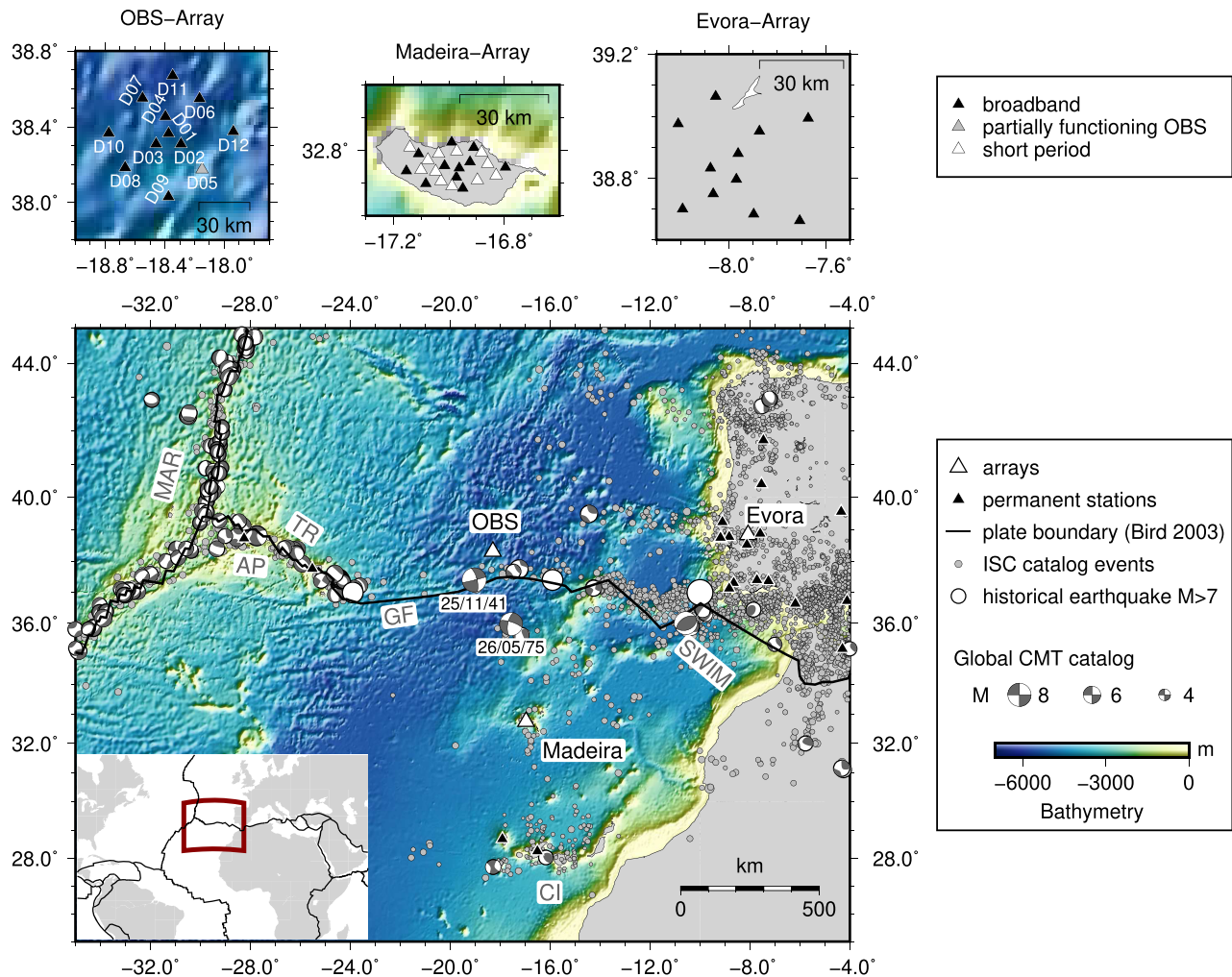


Figure 1. Map of the study region. Lower panel: dots correspond to earthquakes from the ISC catalogue (1900–2012), focal mechanisms are from Global CMT catalogue (1980–2012) (Ekström *et al.* 2012). Large white triangles mark the position of the three arrays, small black triangles mark regional permanent stations. Plate boundaries (Bird 2003) are shown as thickened black lines. MAR marks the mid-Atlantic ridge, AP the Azores Plateau, TR the Terceira Rift, GF the Gloria Fault, SWIM the Southwest Iberia Margin lineaments and CI the Canary Isles. Upper panels show the stations of the three arrays, where broad-band stations are marked by black triangles, short period stations with white triangles and an only partially functioning OBS station with a grey triangle.

DOCTAR is located only about 100 km north of the Gloria fault central between the Azores Islands in the West and Portugal mainland in the East in a distance of about 9° and 11° , respectively (see Hensen *et al.* 2019, for a general description of the Azores–Gibraltar Fracture Zone). The Azores Islands are of volcanic origin and mark the triple point connecting the Eurasian, African and North American plates. The spreading rate between the North American and the Eurasian and African plates is $2\text{--}3\text{ mm yr}^{-1}$ (Argus *et al.* 2011), so that the age of the Eurasian Plate at the latitude of DOCTAR is about 75–80 Myr (Müller *et al.* 2008). Additional extension and strike slip deformation occurs along the Terceira Rift (Fig. 1, TR) north of the Azores Plateau (Fig. 1, AP), which accommodates transtensional motion to the east of the mid-Atlantic ridge (e.g. Bufo *et al.* 1988; Madeira *et al.* 2015). The Gloria fault (Fig. 1, GF) is a major right lateral transform fault separating the oceanic part of the Eurasian Plate from the oceanic part of the African Plate. The relative drift rate along the fault is estimated to be 5 mm yr^{-1} (Fernandes *et al.* 2003; Serpelloni *et al.* 2007).

Between the Gloria fault and the Gibraltar Arc in the East transition to oblique plate convergence occurs (e.g. DeMets *et al.* 2010)

and faulting appears more distributed associated with predominantly reverse and strike-slip faulting (Custodio *et al.* 2016). Fig. 1 shows the ISC catalogue seismicity (ISC 2015) since the beginning of the last century together with focal mechanisms of larger events ($M_w \geq 5.5$) since 1976 from the Global CMT catalogue (Ekström *et al.* 2012). We added furthermore the focal mechanisms of the Gloria fault M_w 8.3 event of 1941 (Baptista *et al.* 2016) and that of the M_s 7.9 1975 North Atlantic earthquake (Lynnes & Ruff 1985) to the map. Historical earthquakes with magnitudes larger than 7 are also shown as large white circles, among them highly destructive earthquakes like the 1755 Lisbon earthquake (Udias *et al.* 1976). Fig. 1 also shows that the seismicity is concentrated in the West on the boundaries of the Azores plateau and the Gloria fault and in the east to a broader belt ranging from Gibraltar to the shelf boundary, here indicated by lighter colours in the bathymetry. The central part of the Gloria fault is, however, absent of $M \geq 5$ events. Interestingly, diffuse seismicity can be found spread over nearly all the oceanic regions, and especially in northeastern direction and around Madeira in the south. The seismicity is recorded routinely and analysed by networks run by IPMA (Instituto Português do Mar

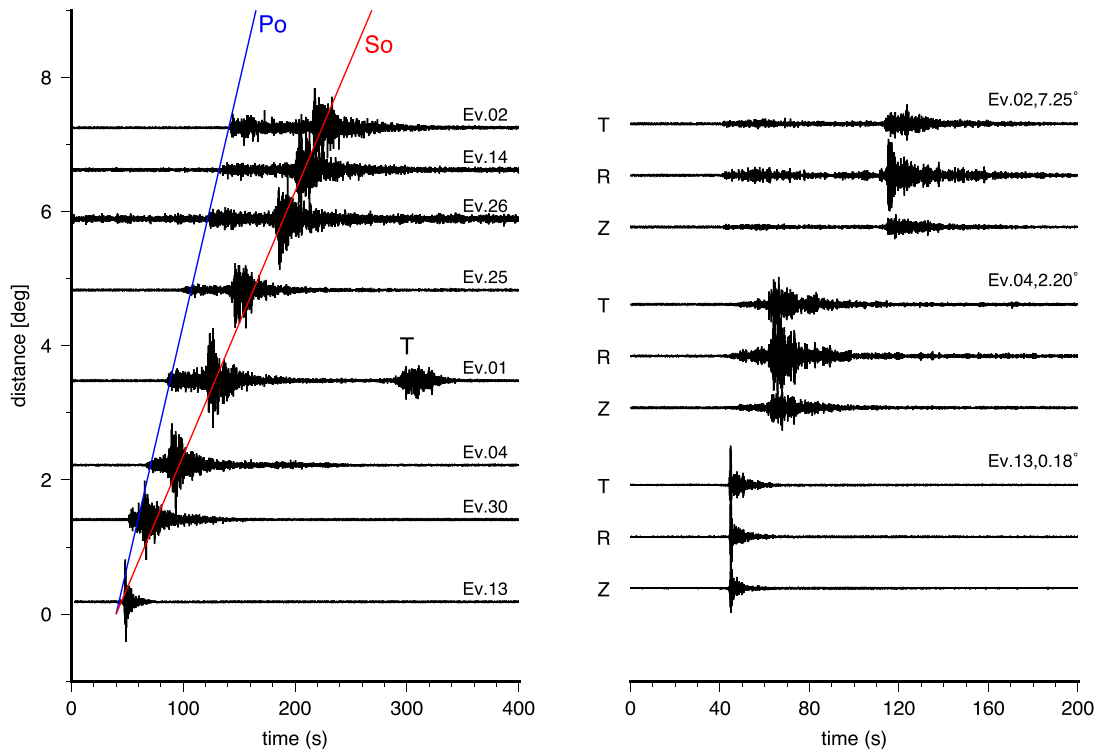


Figure 2. Example events recorded at station D02. (a) Events from eastern direction (only vertical component) as function of distance. Event numbers on the right of the seismograms mark the events according to Table 1. A Butterworth bandpass filter between 4 and 25 Hz (order 3) was applied. The blue line (label Po) corresponds to a velocity of 8 km s^{-1} (P wave), the red line (label So) corresponds to a velocity of 4.37 km s^{-1} ($v_p/v_s = 1.83$). ISC catalogue origin times were aligned. (b) Examples for the component recordings. Events numbers according to Table 1 and distances with respect to OBS station D01 are marked on the right of the seismograms. A Butterworth bandpass filter between 4 and 25 Hz (order 3) was applied and all first onsets were aligned at relative time 40 s.

e Atmosfera) in Portugal mainland, on the Azores and on Madeira with interstation distances of up to 1000 km and more. Phase picks are also provided to the ISC. Because of the lack of stations in the ocean it is not surprising that the magnitude of completeness in the ISC is around $M_L = 3$ and that the location accuracy is not high in the central parts of the oceanic plates.

After recovery of the ocean bottom stations (OBSs) visual inspection of the data revealed a large number of high frequency arrivals, see Figs 2 and 3, for examples. Contrary to continental settings, the OBS record frequencies with more than 30 Hz for micro-earthquakes in more than 500 km distance. The arrivals show typical characteristics of so-called Po and So wave trains (Linehan 1940; Walker & Sutton 1971; Mallick & Frazer 1990; Kennett & Furumura 2013). They travel with oceanic Pn (Po) and oceanic Sn (So) propagation velocities of about 8 and 4.7 km s^{-1} , respectively. The So arrival has typically larger amplitudes on the horizontal components than on the vertical (see Fig. 2b), which is also different to typical continental recordings. The main energy of the Po and So wave trains is in the frequency band from 4 to 25 Hz. Onsets of Po and So are gradual and non-impulsive (see Fig. 3). The long coda of Po and So wave trains, which is a third untypical characteristics of these phases, has been explained as waves scattered in the whole oceanic lithosphere (Mallick & Frazer 1990; Kennett & Furumura 2013; Shito *et al.* 2013).

Our paper has two different aims, (1) to understand the nature and distribution of the oceanic intraplate seismicity in the Northeast Atlantic, which is measured the first time with such a high resolution and (2) to adapt and test array seismological techniques for the problem of micro-earthquake detection and location using a

medium aperture ocean bottom array and evaluate its performance in comparison to an ocean island and a continental array.

Our manuscript is organized as follows: after description of the data and the method to detect Po and So arrivals using an array seismological approach and presentation of results regarding observed velocities, frequencies and signal shapes, the array backazimuth and the time difference between So and Po arrivals is used to locate those events for which both arrivals can be detected. We compare the results with the catalogue seismicity, for example which catalogue events are detected by the ocean bottom array and which not, and which new events can be found by the ocean bottom array only. We locate events near and beneath DOCTAR using a backprojection approach and constrain for two larger events their focal mechanisms. We discuss the tectonic implications of the newly found seismically active regions in the northeastern Atlantic lithospheric Plate which were not imaged before.

2 DATA AND LOCAL SITE CONDITIONS

The stations installed in the deep sea are free fall ocean bottom stations of the German DEPAS (Deutscher Geräte-Pool für amphibische Seismologie/German instrument pool for amphibian seismology) instrument pool and are equipped with Guralp CMG 40T (60 s eigenperiod) three-component sensors, broad-band hydrophones of type HTI-04-PCA/ULF and Send Geolon MCS recorders (Stähler *et al.* 2016; AWI *et al.* 2017). For the sampling frequency of 100 Hz the nominal dynamics of the recorder is 21 bit. The OBS array has been deployed and recovered with the German research vessel RV

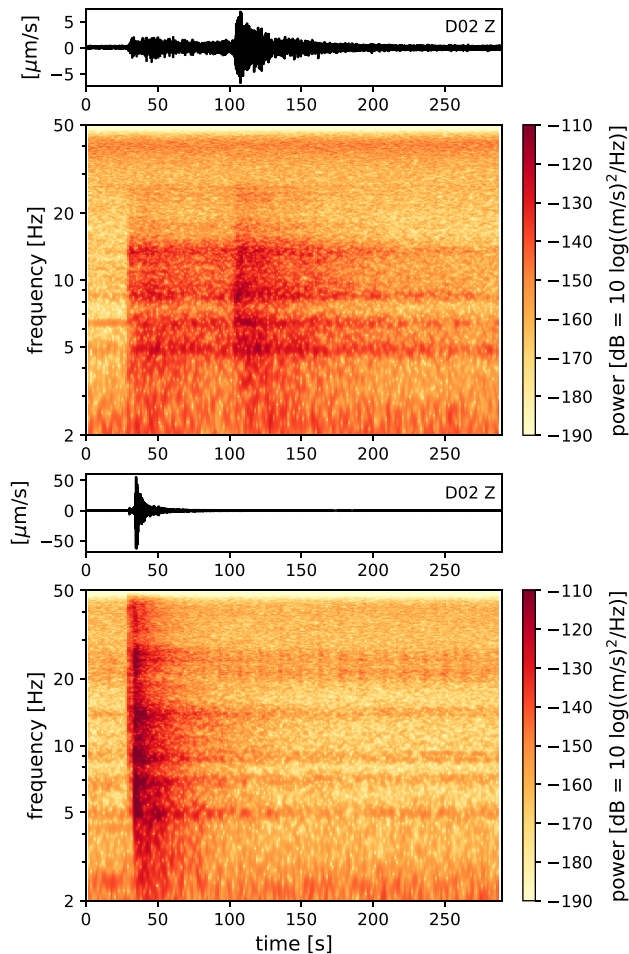


Figure 3. Spectrograms for the vertical component of station D02. Lower panel: local event (event 13, see Table 1), upper panel: far regional event (event 02, see Table 1). A Butterworth highpass at 2 Hz was applied to the traces before calculating the spectrogram to suppress the high amplitude ocean microseisms.

Poseidon (RV Poseidon cruises POS416 and POS431). After recovery of the 12 stations it turned out that one of the stations (D05 in Fig. 1) had only one undistorted horizontal component due to strong inclination of the OBS station frame at the landing point of the OBS.

Timing problems of two other stations could be solved using an ambient noise based cross-correlation technique (Hannemann *et al.* 2014). The three-component stations were oriented using *P* waves and Rayleigh waves of teleseismic events (Hannemann *et al.* 2017).

The topography within the array reaches about 800 m, ranging from 5200 m water depth to about 4400 m water depth. Rough basement topography with sediment filled depressions is seen on analogue seismic recordings of the area under investigation which were recorded in 1969 (NOAA 1969). Hannemann *et al.* (2016) used the frequency dependence of apparent *P*-wave incidence angles to infer on the *S*-wave velocity structure and found sediment layer thicknesses between 0.3 and 0.9 km and *S*-wave velocities between 0.7 and 1.4 km s⁻¹. The crustal thickness was estimated between 4 and 10 km with *S*-wave velocities ranging from 3.5 to 4.3 km s⁻¹. The revealed uppermost mantle *v_s* values are high (*v_s* > 5 km s⁻¹ in some cases) with a tendency to increase towards the Gloria fault. About 150 km to the west of station D01 of the DOCTAR array

a 150-km-long seismic profile across the Gloria fault also shows rough topography and thin sediments partially thickened in local depressions and by about 10 per cent decreased *v_p* and *v_s* velocities in an about 4-km-thick layer beneath the oceanic lower crustal layer which is interpreted as either locally thickened oceanic lower crust or (preferred by the authors) serpentinized mantle as a result of hydration (Batista *et al.* 2017).

Madeira Island, where the second array is placed, is an intraplate volcanic island, located about 700 km west of the African coast. The topography is very rough and the mountains reach an altitude of 1861 m. The island is listed as hotspot evidenced by seismic tomography and isotope geochemistry (Hoernle *et al.* 1995; Mata *et al.* 1998). No historical eruptions are documented on the island, however, the volcanism is classified as active and is divided into three main volcanic stages starting about 5.6 Ma, a main building stage 2.5–1.0 Ma and more recent activity till 6–7 ka (Geldmacher *et al.* 2000, 2005; Klügel *et al.* 2009). The upper crustal structure was recently investigated using ambient noise techniques where lower velocities were found in the uppermost layers of the western part of the island and beneath the highest mountains more to the east, the latter embedded in a zone of higher velocities (Matos *et al.* 2015). On the island of Madeira the deployed array consists of 9 broad-band stations of type Guralp CMG 40T (60 s eigenperiod), 3 broad-band stations of type STS2 (120 s eigenperiod) and 12 mid-period sensors of type Lennartz LE-3G (5 s eigenperiod). The orientation of the stations was determined using a gyro-compass because magnetic orientation turned out to be problematic due to iron-rich volcanic material. While for most stations, especially in the eastern part of Madeira the misorientations scattered with at most ±5° around the declination value of 345°, deviations reached up to +28° in the western part of Madeira.

The third array in western Portugal near Evora consists of 12 irregularly distributed stations equipped with Guralp CMG 40T (60 s eigenperiod), also operated at 100 Hz sampling rate. The stations were oriented with magnetic compass. The array is situated on metamorphic rocks of neoproterozoic and lower palaeozoic age of the Ossa Morena zone near the seismically active east–west striking Moura-Vidigueira fault and the longer Messejana fault striking NE–SW (Borges *et al.* 2001; Matos *et al.* 2018). A few focal mechanisms obtained for this area show strike-slip characteristics (Borges *et al.* 2001).

3 ARRAY PROCESSING METHODS

3.1 Plane-wave approach

The aperture of DOCTAR is about 70 km and a wavelength criterion considering apparent velocities of upper mantle phases of about 8 km s⁻¹ (*P_o*) and 4.7 km s⁻¹ (*S_o*) demand a signal dominant period of at least 10 s. Thus, the ocean bottom array is much too large to analyse the observed 4–30 Hz *P_o* and *S_o* arrivals with standard array techniques (Rost & Thomas 2002; Schweitzer *et al.* 2012). To avoid strong aliasing effects the signals were transformed to more long-period waveforms, using so-called non-linear beam forming. Such methods have been used for onland seismological arrays before (Gibbons *et al.* 2008), and were successful if impulsive, isolated phases are present.

We pre-filtered the continuous data with a third order Butterworth bandpass between 4 and 25 Hz. Then, two subsequent methods have been tested: (i) a short-term over long-term average (STA/LTA) approach was used with a STA window of 2 s length and a LTA

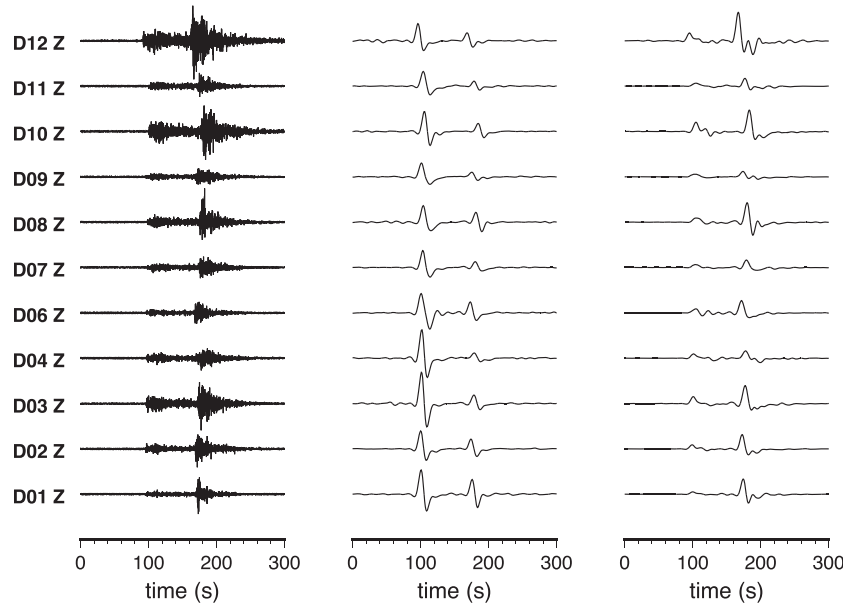


Figure 4. Incoherent beamforming pre-processing. Left-hand panel: waveforms of event 02 (see Table 1) bandpass filtered between 4 and 25 Hz (Butterworth filter of order 3). Middle panel: STA/LTA characteristic functions low passed with acausal Butterworth filter with corner period of 15 s. Right-hand panel: envelope traces low passed with acausal Butterworth filter with corner period of 15 s.

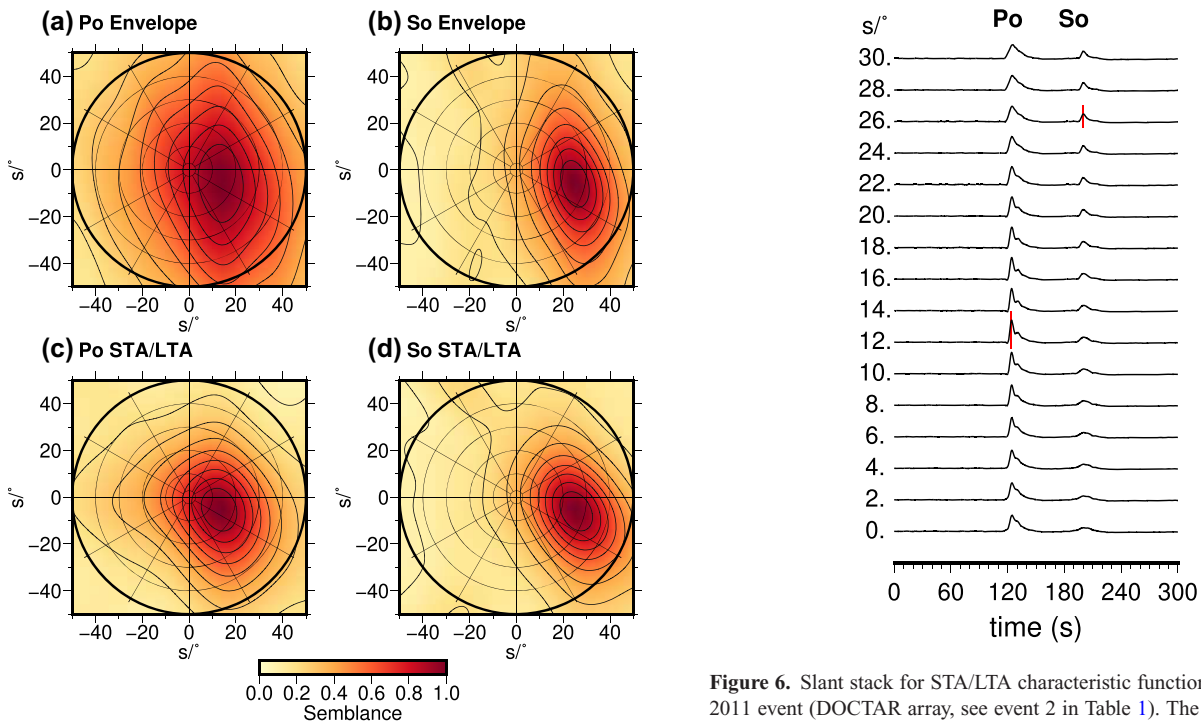


Figure 5. Frequency–wavenumber processing result for Po (left-hand panels) and So (right-hand panels) for event 02 (see Table 1). Panels (a) and (b) show results for the envelope characteristic functions, (c) and (d) show results for the STA/LTA characteristic functions.

window of 30 s length, followed by differentiation and low pass filtering; (ii) the envelope of the traces was computed, differentiated to get two-sided wavelets and lowpass filtered with a 0.067 Hz (15 s) Butterworth filter of third order as in (i). Subsequently (for both approaches) the filtered traces were normalized with respect to the maximum amplitude within the analysis window and processed with a broad-band frequency–wavenumber analysis tool in the frequency

Figure 6. Slant stack for STA/LTA characteristic functions for the 22 July 2011 event (DOCTAR array, see event 2 in Table 1). The maximum found for Po -slowness and So -slowness are marked by red vertical bars and are used to calculate the difference traveltime between So and Po .

band of 0.02–0.1 Hz for horizontal slowness values up to 50 s deg^{-1} to calculate a semblance coefficient (Neidell & Taner 1971) as function of slowness and backazimuth.

In frequency domain broad-band semblance can be defined as:

$$s = \frac{\sum_{j=1}^M [\sum_{k=1}^N v(\vec{r}_k, \omega_j) e^{i\omega_j(\vec{r}_k - \vec{r}_0) \cdot \vec{u}}]^2}{\sum_{j=1}^M \sum_{k=1}^N [v(\vec{r}_k, \omega_j)]^2} \quad (1)$$

Here M and N are the number of frequency samples and the station number, respectively, $v(\vec{r}_k, \omega_j)$ are the Fourier transformed

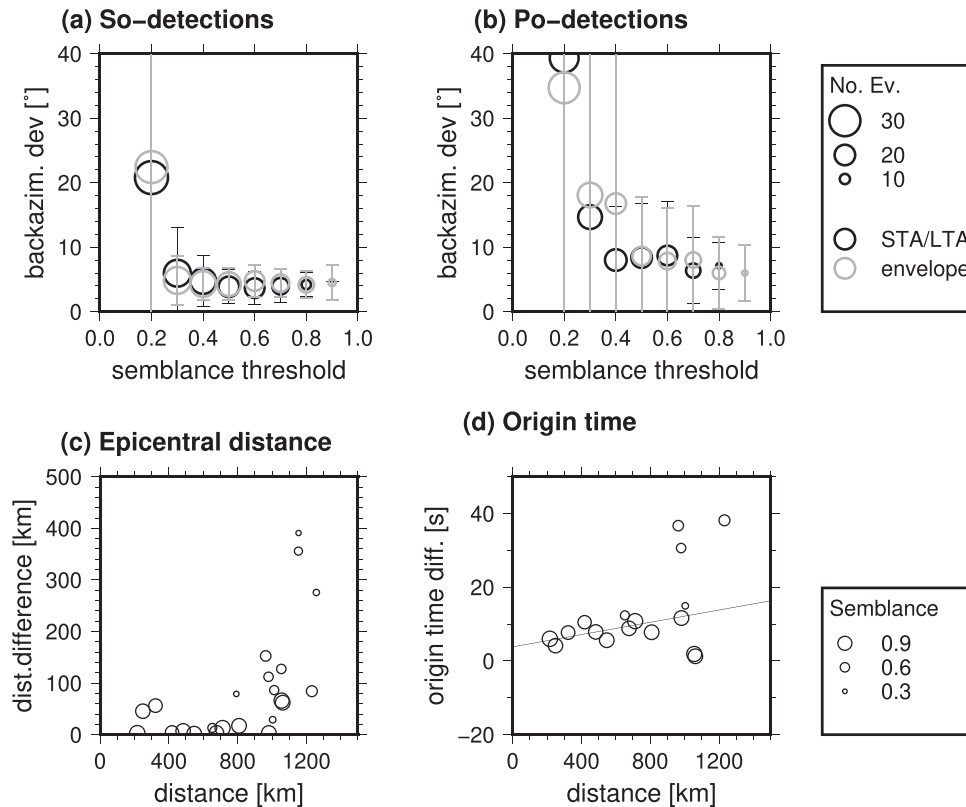


Figure 7. Deviations between true and estimated backazimuth for 32 selected regional events as function of detection semblance threshold. (a) Results for *So*-wave detections, (b) results for *Po*-wave detections. Black colour marks results using the low pass filtered STA/LTA characteristic functions, grey colour marks results using the low pass filtered envelope function, respectively. Error bars correspond to standard deviations. (c) Circles correspond to the epicentral distance difference between the catalogue position and the distance estimated using $v_{Po} = 8.29 \text{ km s}^{-1}$ and $v_{So} = 4.71 \text{ km s}^{-1}$ from *Po* and *So* arrival times (see Fig. 6) at the DOCTAR array. (d) Difference between catalogue origin time and the origin time calculated from the *So* arrival time and a shear wave velocity of $v_{So} = 4.71 \text{ km s}^{-1}$. The line fit (straight line) for this difference corresponds to $\delta t_{\text{origin}} = 0.0083 \cdot \Delta[\text{km}] + 3.83 \text{ s}$.

characteristic functions (filtered STA/LTA traces or trace envelopes) at station k phase shifted by $e^{i\omega_j(\vec{r}_k - \vec{r}_0)\vec{u}}$, where \vec{u} is the horizontal slowness and \vec{r}_k and \vec{r}_0 are the location vectors of station k and a reference station.

In each case the analysis window length was 30 s and the time windows were continuously shifted by 1 s time steps. A detection was declared if the semblance value is three times higher than the average semblance value in the 100 s time window ahead of the analysis window.

Fig. 4 shows two different processing steps for one example event. The STA/LTA approach enhances and detects the *Po* arrivals, which have much smaller amplitudes than *So*. However, the *So* arrivals are still detected on all three components. In contrary, the envelope approach produces strong *So* arrivals, but has often *Po* arrivals too weak to be automatically detected.

For the high frequency band used for the pre-filtering (4–25 Hz) differences in the signal-to-noise ratio between the three sensor components are small. We used therefore all three components together in a single frequency–wavenumber analysis processing, adding an additional factor of $\sqrt{3}$ to the noise suppression. Figs 5(c) and (d) shows results for the *Po* and the *So* wave train, respectively, for the 22 July 2011 event (event 2 in Table 1) using the STA/LTA characteristic function. The azimuth and slowness is in both cases well resolved. In contrast, the frequency–wavenumber analysis using the envelope characteristic functions shows a much broader maximum for the *Po* arrivals compared to the STA/LTA result, whereas the result for the *So* arrivals is similar (Figs 5a and b).

The distance to the events can be estimated using the time difference between *So* and *Po* arrivals. Fig. 6 shows the result for a slant stack of characteristic function traces using the backazimuth estimated from the *So* arrival, where we used a stack of undifferentiated (one-sided) characteristic functions of all three seismometer components. This allows more precise automatic calculation of *So*–*Po* difference times than the differentiated versions used in the detection processing, because the position of the maximum of the undifferentiated characteristic function at the *So* onset is less influenced by *Po* coda. *Po* and *So* can be easily identified by their different slowness and the arrival time difference can be estimated from the difference time of the maxima of the characteristic functions. For events at large distance compared to the hypocentre depth, the epicentre of the event is then determined using the *So* backazimuth and the distance calculated from *So* to *Po* difference traveltimes. Finally the origin time is calculated from the distance and the wave velocities (here we used v_{So}). This procedure does not allow to resolve the hypocentre depths of the events.

3.2 Backprojection approach

Frequency–wavenumber analysis relies on the plane wave assumption, implying that no events within the array or near the array can be detected with unbiased azimuth and slowness parameters. For smaller distances ($< 2^\circ$), the long-period filtering will also lead to an interference of *Po* and *So* resulting in difficulties to separate the

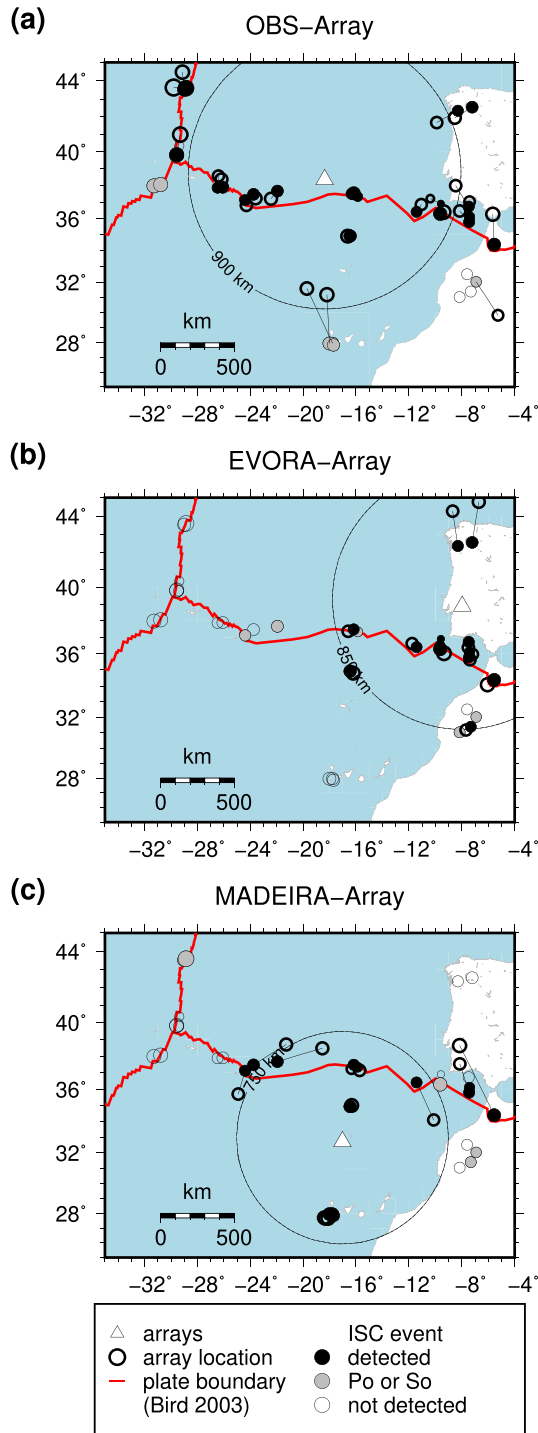


Figure 8. Detection and location results for test event data set (see Table 1). Full black circles mark the catalogue positions of events which were detected and could be located. Empty black thick line circles mark the positions at which the events were located by the respective array. Grey circles mark events where only one onset (*Po* or *So*) was found. Empty black thin line circles mark events which were not detected at all. (a) Results for OBS array, (b) results for EVORA array and (c) for the MADEIRA array. Large black circles mark approximately the detection/location distance ranges for each array.

two onsets. We used a different approach for such events, where we calculated interstation delay times for *P* and *S* wave arrivals based on a 1-D velocity model for each hypothetical source point in a volume grid. The arrival times were used to backproject the energy in a specific time window to the corresponding gridpoint by shifting the filtered STA/LTA characteristic waveforms for each array station. A semblance coefficient is then calculated as

$$s(t_0) = \frac{\sum_{j=1}^M [\sum_{k=1}^N v(\vec{r}_k, \omega_j, t_0)(e^{i\omega_j t_k^P} + e^{i\omega_j t_k^S})]^2}{\sum_{j=1}^M \sum_{k=1}^N v(\vec{r}_k, \omega_j, t_0)^2 (e^{i2\omega_j t_k^P} + e^{i2\omega_j t_k^S})^2}, \quad (2)$$

where the summation is over M frequency samples, N is the number of all traces (Z, N, E), $t_k^{P,S}$ is the propagation time of *P* and *S* wave first arrivals in the local CRUST1.1 model (see Table 2) from a specific gridpoint to station k , t_0 is the assumed source origin time and $v(\vec{r}_k, \omega_j, t_0)$ is the Fourier transformed filtered characteristic function at station k in a time window with length T_{wdw} between $t_0 + t^{Pref} - T_{wdw}/2$ and $t_0 + t^{Pref} + T_{wdw}/2$ (t^{Pref} is the *P*-wave traveltimes to the reference station D01 in the centre of the array). In case of a true source point the shifted and normalized characteristic functions for *P* and *S* waves align in time and show a high semblance coefficient (G34; Grigoli *et al.* 2013). Due to high computation times for extended grids, a two step approach was used. In a first step a long-period filter (10 s) was applied to lowpass the STA/LTA characteristic functions. We used a grid ranging from 36.4°N to 40.4°N in latitude and 20.4°W to 16.4°W in longitude with a step size of 0.2°. The depth was sampled between 0 and 50 km with a step increment of 10 km. The time step was 1 s for the complete data set. The highest semblance value with its specific grid coordinates was stored for each time step and finally a list of possible event detections was produced using a sliding window of 2 s length and a semblance threshold value of 0.2 above a moving average of 60 s length. In the second step each detection was analysed using a finer grid of $\pm 0.5^\circ$ around the detection coordinates of the first processing step with lateral step size of 0.05° in latitude and longitude and 2 km in depth between 0 and 70 km depth. The time increment here was 0.1 s and the low pass filter applied to the STA/LTA characteristic functions had a corner period of 2 s.

4 DETECTION AND LOCATION PERFORMANCE

4.1 Array location technique performance

We selected 32 regional events which occurred during the common recording time of all three arrays. This set of test events has larger magnitudes and is according to ISC catalogue parameters rather well located (see Table 1 and Fig. 8 for the locations). Figs 7(a) and (b) show a comparison of their theoretical backazimuths and the backazimuths of *So* and *Po* array detections at DOCTAR as function of the semblance threshold used to declare a detection. We tested again both incoherent beamforming approaches, that is using low pass filtered STA/LTA characteristic functions versus low pass filtered envelope functions. Inspection of Figs 7(a) and (b) show that backazimuths of *Po* waves are less accurate than those of *So* waves. Overall also the number of detections is lower for *Po* (indicated by smaller symbol size in Fig. 7b). Backazimuth residuals and standard deviations are comparable for both methods. A semblance detection threshold of 0.4 seems to define a good compromise between a high number of *So* and *Po* detections and low backazimuth residuals with about 5° deviation for *So*-arrivals and about 8° deviation for *Po* arrivals. The number of events is too small and the azimuthal

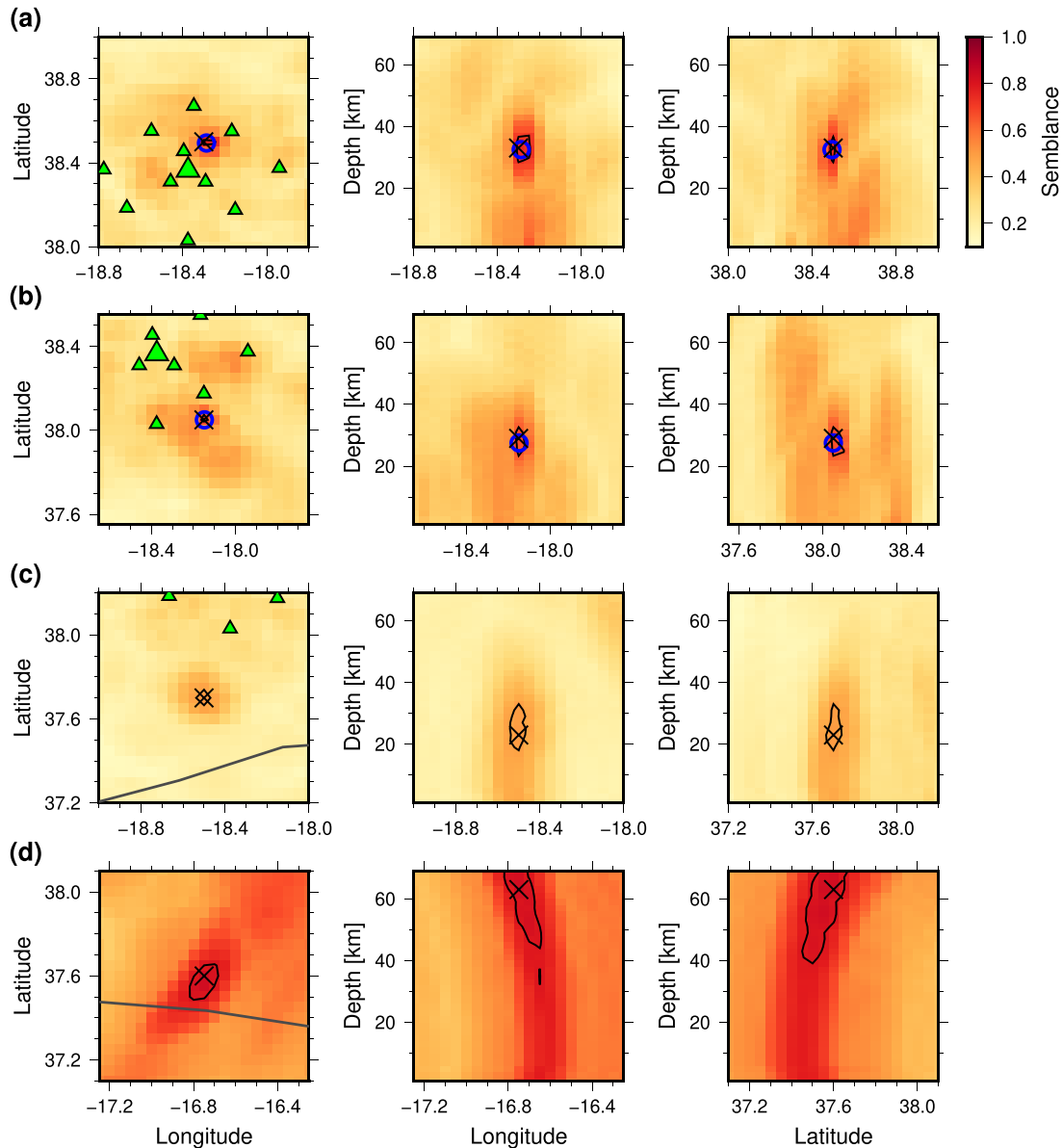


Figure 9. Location examples using the backprojection approach. Shown are slices through the semblance volume for latitude and longitude (first column), latitude and depth (second column) and longitude and depth (third column). The semblance maximum is marked by a black cross. Circles mark the hypocentre position determined from picked onsets using the HYPOSAT software (Schweitzer 2001). A black isoline marks the semblance contour for a -0.05 decrease with respect to the semblance maximum, which is used for relative error estimation. Stations of the DOCTAR array are marked by triangles. An enlarged triangle marks the central station D01, the plate boundary is marked by a grey line. (a) Results for the event on 27-OCT-2011 21:32:46.2 (M_L 1.6) at an epicentral distance of 16.4 km from station D01. (b) Results for the event on 19-SEP-2011 05:37:45.2 (M_L 2.1) at 40.1 km distance. (c) Results for the event on 24-AUG-2011 19:25:41.7 at a distance of 74.6 km. (d) Results for the event on 25-SEP-2011 21:31:26.7 (M_L 2.5) at 166.1 km epicentral distance. Event parameters can be found in Table 6.

coverage is too limited to allow conclusions regarding azimuthal or distance dependent patterns in the residual distribution.

The better results for S_o backazimuths can be explained by the smaller apparent velocities and thus longer delay times for S_o waves across the array stations. Therefore biases due to effects of station specific structure on the traveltimes or the waveform shapes have likely less influence than in the case of P_o waves (Schweitzer *et al.* 2012). Characteristic functions based on STA/LTA represent better high frequency phase onsets, while those based on envelopes represent the arrival of largest amplitudes of the low-pass filtered wave trains. The slightly better performance of the STA/LTA approach

indicates that the variability of high frequency onsets is more coherent for the DOCTAR array. However, it is beyond the scope of this study to optimize the parameters of each approach systematically, we therefore decided to use the STA/LTA characteristic functions in the following analysis. High quality P_o arrivals are observed for 17 of the 32 selected events and could be used to determine the epicentre distance and the origin time. The best match between epicentres and origin times from the catalogue and those estimated at DOCTAR was reached using P_o and S_o velocities of $v_{P_o} = 8.29 \text{ km s}^{-1}$ and $v_{S_o} = 4.71 \text{ km s}^{-1}$. Fig. 7(c) shows the distance errors relative to the distances to station D01 calculated with the catalogue locations

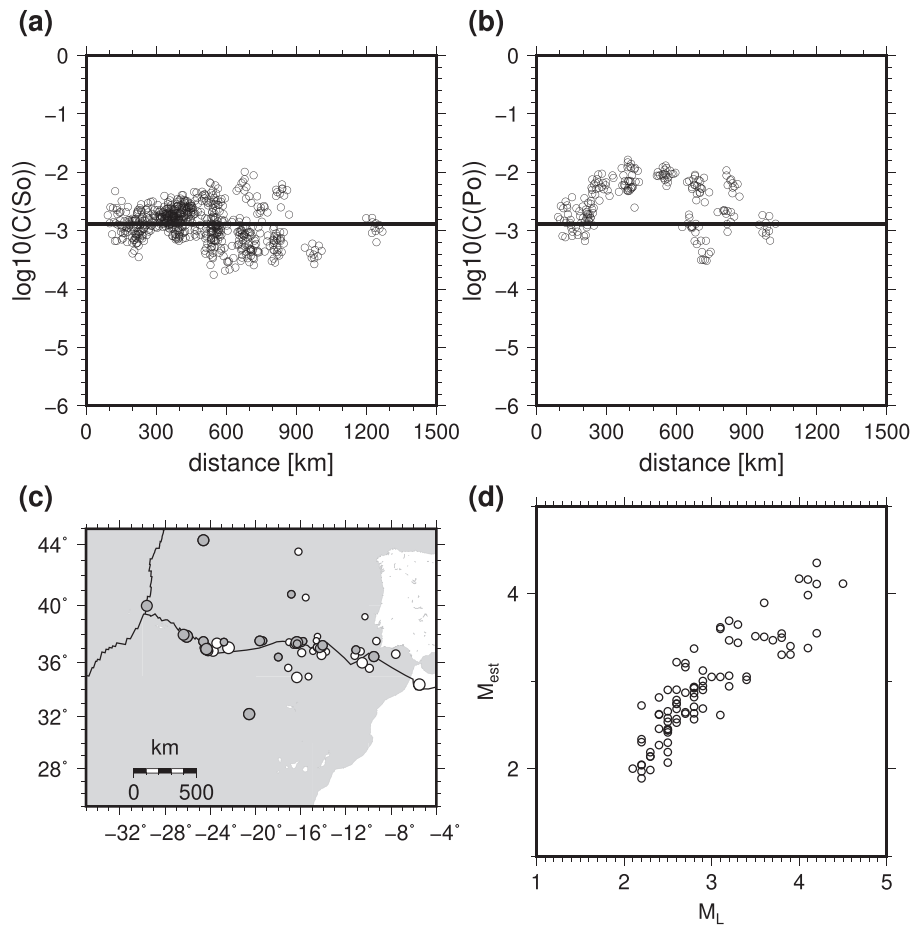


Figure 10. (a) Constant $\log_{10}C$ in eq. (4) as function of distance to DOCTAR station D01 for 58 events located by the permanent network stations with S_o wave signal-to-noise ratio ≥ 3 at the OBS array stations. Amplitudes were corrected by station specific correction terms (see Table 3). (b) as (a) but for P_o amplitudes (signal-to-noise ratio ≥ 2 , 19 events). (c) Locations of the events used to calculate $\log_{10}C$. White circles mark the events used to calculate $\log_{10}C(S_o)$, darkgrey circles correspond to the events used to calculate $\log_{10}C(P_o)$. (d) Estimated M_L magnitudes as function of catalogue M_L magnitudes.

(open circles in Fig. 7c). Up to a distance of about 900 km the distance mismatch is on average 1.5 km with a standard deviation of 25 km. For larger distances the distance mismatch increases with an average of 37 km and a standard deviation of 78 km. Fig. 7(d) shows the mismatch of the estimated origin times compared to the catalogue origin times. The straight line fit in Fig. 7(c) for the origin time mismatch corresponds to $\delta t_{\text{origin}} = 0.0083 \Delta [\text{km}] + 3.83 \text{ s}$ and compensates partially the bias due to the neglectance of the event depth.

Fig. 8 summarizes the detection and location performance of the different arrays for the regional test events. From Fig. 8(a) it is obvious that the events in the interior of the oceanic plate are detected by the OBS array and located with reasonable accuracy up to a distance of about 900 km. In the East events on the continent or continental shelf are either not detected at all or show a pronounced bias in distance (2 events in northern Spain) or a large azimuthal bias (events near southern Portugal, Gibraltar and Morocco). For the test events near the Canary Island only S -wave onsets are detected. These are better visible at the Madeira array (Fig. 8c). Here events which are farer away than about 750 km are either not or only weakly observed. Remarkable is the strong azimuth deviation observed for events in the northwest and northeast of the array. This is likely caused by the elliptical shape of the Madeira array (see Fig. 1) with a larger aperture in east–west than north–south direction. For the

Evora array detection and location results are reasonable for events within about 800 km distance (Fig. 8b). It should be mentioned that the comparison of the location capabilities of the three arrays is not fully fair because no attempt was made to determine the best-fitting wave velocity combinations and origin time corrections for the Madeira and the Evora array. In this test we also neglected the obvious difference between oceanic and continental parts of the travelled paths, because in this study we are mainly interested in events located within the oceanic lithosphere. It is therefore not surprising that two events in the North of Portugal are shifted to larger distances using the Evora array and to too short distances using the DOCTAR array, because the slower continental crust was not taken into account.

4.2 Backprojection location technique performance

We could not design a similar location accuracy test for the backprojection approach used to locate the events near to the DOCTAR array, because no well located catalogue events were available in the recording time span of the experiment. In Fig. 9 we show the backprojection semblance maps for four events in three different spatial orthogonal slices. The events are located in increasing epicentral distance with respect to station D01 ranging from 16.4 km up to 166.1 km, see the figure caption and Table 6 for the event

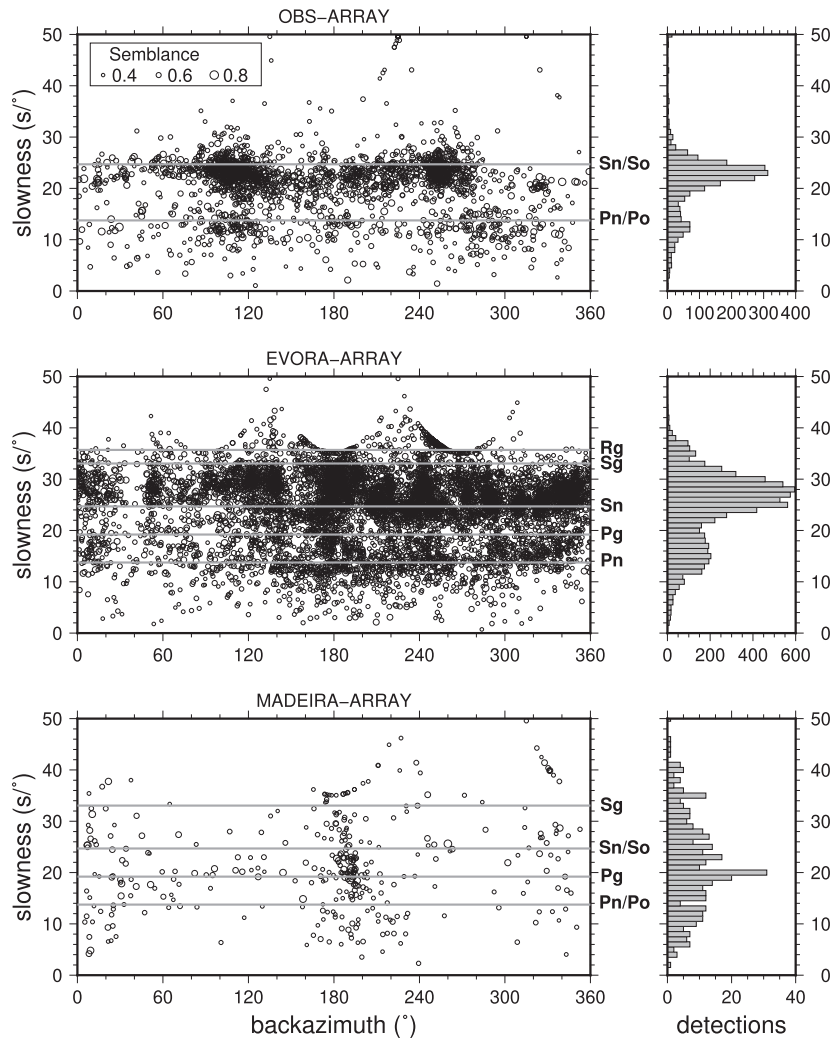


Figure 11. Detected onsets for the three arrays. The symbols scale with the semblance maximum found for the specific onset. (a) Ocean bottom array, (b) Evora array, (c) Madeira array. Slownesses of Pn, Pg, Sn and Sg, Rg for a surface focus (PREM) are marked by grey bars. Histograms on the right depict mean slownesses of the different wave types.

parameters. The event shown in Fig. 9(a) is located well within the DOCTAR array and the semblance maps show a central peak concentrated in all three spatial dimensions. An open circle in Fig. 9(a) marks the hypocentre position determined from picked onset times using the HYPOSAT software (Schweitzer 2001) and the same velocity model as was used for the backprojection. Both positions match well. The event shown in Fig. 9(b) has a smaller magnitude and is located slightly out of the outer ring of the DOCTAR array (epicentral distance to station D01 is 40.1 km) with a still well defined peak in the semblance maps, a statement that also holds for the event shown in Fig. 9(c) at a distance of 74.6 km from D01. At a distance of about two array apertures (see Fig. 9d for an event in 166.1 km distance) the peak in the semblance maps starts to become broad and especially the hypocentre depth resolution deteriorates drastically.

4.3 Magnitude determination

For most events recorded at the OBS array standard M_L determination is difficult because surface and body wave energy is practically absent in our ocean bottom recordings between 0.5 and 4 Hz, and

empirical attenuation functions are missing for higher frequency So phases. We therefore decided to use a set of 79 reference events with magnitudes between M_L 2 and 4, which were observed in common by the permanent network on land and the OBS array, to derive own empirical attenuation curves. M_L values were taken from the ISC catalogue and from bulletins and are based on Carrilho & Vales (2009). The 79 common events were also locatable with good quality with DOCTAR with a signal-to-noise ratio of at least 3 at 10 array stations in the passband 4–25 Hz. We calculate the epicentral distances to each array station i and measured for every event j and station i the vector peak amplitudes $A_i^{(j)}$ of the So and Po wave trains filtered between 4 and 25 Hz. Additionally, for every reference event j the average peak amplitude across the array is calculated, $\langle A \rangle_j = (\sum_{i=1}^M A_i^{(j)})/M$, where M is the number of array stations. Since the epicentral distance between the reference earthquakes and the array is much larger than the interstation distance, the array measurements may be viewed in first order as a single point measurement at the array centre given by the average peak amplitude within the array. A systematic deviation of single station peak amplitudes against the array average indicates a station site

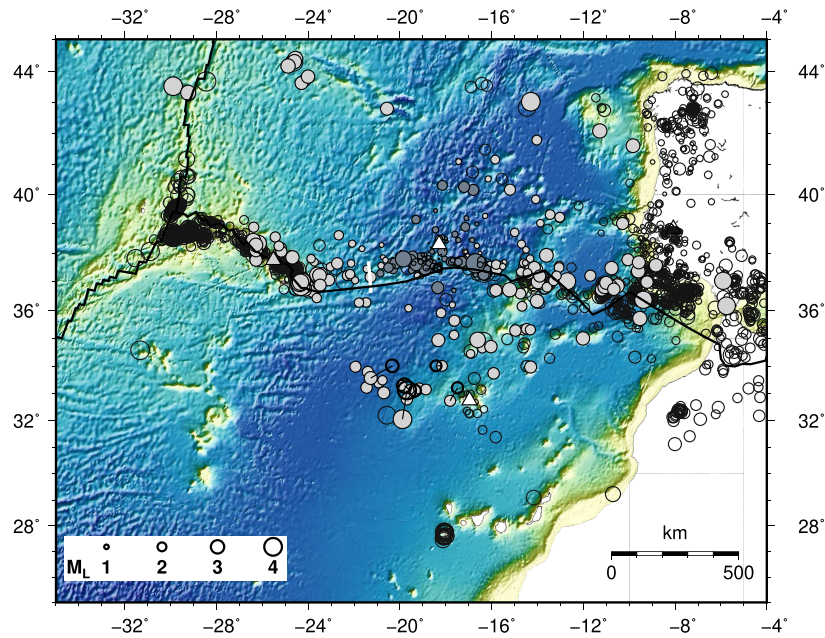


Figure 12. Event epicentres localized by the OBS array. Lightgrey circles mark the locations obtained with the DOCTAR array with the plane-wave approach, while darkgrey circles correspond to the locations obtained using the backprojection approach. Open black circles mark the positions of all events in the regional catalogue published by PDA and INMG in the timespan of the experiment (4 July 2011 to 20 April 2012). Open black thick line circles mark the locations of events where in addition to the DOCTAR array direction and traveltimes, traveltimes and directions observed at the Madeira array could be used in the location procedure. White triangles mark the position of the DOCTAR array and the array on Madeira, a light grey triangle marks the permanent station CMLA on the Azores. The white line shows the position of a seismic profile in the study region (Batista *et al.* 2017).

effect. We estimate the station site factors w_i by

$$w_i = \sum_{j=1}^N \frac{A_i^{(j)}}{\langle A \rangle_j}, \quad (3)$$

where N is the number of reference events. The station site factors are listed in Table 3. Most of the correction terms do not deviate much from 1. Only station D10 shows in the passband amplitudes which are higher by a factor of about 1.5 than the average amplitude of all stations, while station D11 shows amplitudes lower by about a factor of 2. Remarkably there is no significant difference between site effects determined for So and Po waves, respectively.

The IASPEI formula for M_L is given as

$$M_L = \log_{10}(A^{WA}) + 1.11 \log_{10} R + 0.00189 R - 2.09 \quad (4)$$

where R is the hypocentral distance in km and A^{WA} is the Wood–Anderson instrument amplitude of the S wave maximum (Bormann & Dewey 2013). We set $A^{WA} = CA^{Obs}$ and find for $\log_{10} C$ an average value of -2.8811 ± 0.0253 without a significant distance dependent trend. Fig. 10(a) shows the scatter of $\log_{10} C$ for So amplitudes as function of distance. The scatter increases for distances beyond 600 km. Fig. 10(b) shows $\log_{10} C$ for Po amplitudes. The plot indicates that for distances up to 600 km the geometrical attenuation is almost a factor of $\frac{1}{R}$ stronger for Po waves than for So waves, what is not a factor of a special event distribution (see Fig. 10c). Fig. 10(d) plots the local magnitudes estimated from So amplitudes versus the catalogue M_L .

5 DOCTAR DETECTION AND LOCATION RESULTS

5.1 Observed velocities and characteristics of Po and So wave trains

Fig. 11 shows the detections found for all three arrays as function of slowness and backazimuth. Table 4 lists the arrivals of different wave types detected at the different arrays. Teleseismic body wave arrivals plot at low slowness values ($< 10 \text{ s deg}^{-1}$). For DOCTAR only two slowness ranges are found: Onsets with slownesses between about 10 and 15 s deg^{-1} are associated with Po , onsets with a slowness between about 20 and 26 s deg^{-1} are associated with So arrivals (Fig. 11a). The apparent velocities of these arrivals correspond to typical wave velocities expected for oceanic lithosphere (Hart & Press 1973; Kennett & Furumura 2013). Especially the So arrival slownesses seem to show a backazimuth dependency with low slownesses for northern and southern directions. This indicates a velocity anisotropy within the ocean bottom array and is discussed in another study.

The detection results at the Evora array show a much more complex pattern (Fig. 11b). We find Pn slownesses in the same range as the Po arrivals observed at the DOCTAR array. However, the largest number of detected arrivals has slownesses which correspond with about 28–35 s deg^{-1} to Sg or Rg arrivals. Sn arrivals are especially found for backazimuth directions between about 90° and 280°. The average slowness of Sn arrivals at the Evora array is with about 25 s deg^{-1} slightly higher than the So slownesses found at the ocean bottom array.

Overall much less onsets are detected at the Madeira array. Onsets with Po signature, that is slowness corresponding to upper mantle P -wave velocities are rare. So /Sn type arrivals are more often found where a cluster at southern backazimuths is most prominent. This

Table 1. Test event data set used for analysing the detection and location capabilities of the different arrays. Event parameters are from ISC catalogue (ISC 2015), where the locations are ISC locations and the magnitudes are from different agencies. An exception is event 13 near the OBS array where the parameters represent our own solution. Events only used for exemplary plots in Figs 2 and 3 are marked by a star.

Ev.No	Origin time	[yyyy:mm:dd hh:mm:ss]	Latitude [°]	Longitude [°]	M_L	Depth [km]
01*	06-JUL-2011	10:51:53.5	37.0641	-14.2248	3.0	22.0
02	22-JUL-2011	19:19:32.0	36.2957	-9.6290	4.8	10.0
03	27-JUL-2011	04:48:50.6	35.7947	-7.4387	4.0	10.0
04*	19-AUG-2011	09:02:16.8	37.7911	-15.2098	2.6	10.0
05	20-AUG-2011	13:03:27.8	37.9004	-26.0757	4.2	21.0
06	31-AUG-2011	12:17:27.5	43.6005	-28.8625	5.6	14.9
07	25-SEP-2011	17:29:03.5	37.4881	-16.1728	4.0	10.0
08	01-OCT-2011	07:14:36.8	42.5447	-7.2082	4.2	10.0
09	07-OCT-2011	22:18:27.5	37.8779	-26.4796	3.9	5.2
10	08-OCT-2011	20:34:46.7	27.8568	-17.7135	4.4	15.4
11	19-OCT-2011	06:23:43.7	37.9899	-31.2932	5.0	15.9
12	22-OCT-2011	01:48:22.1	43.5292	-29.0048	4.7	14.0
13*	27-OCT-2011	21:32:46.0	38.5000	-18.3000	0.8	33.0
14*	03-NOV-2011	11:48:52.9	36.0895	-10.4395	4.2	28.8
15	04-NOV-2011	20:36:26.0	27.9677	-17.7766	4.4	23.0
16	08-NOV-2011	22:05:59.8	36.4157	-11.4185	2.8	35.0
17	11-NOV-2011	00:20:14.1	27.9625	-18.0169	4.6	30.5
18	14-NOV-2011	02:02:46.2	37.4818	-23.7566	4.2	6.2
19	14-NOV-2011	10:23:01.7	39.7745	-29.4188	3.7	11.0
20	14-NOV-2011	11:34:57.6	39.8300	-29.5721	5.1	12.8
21	14-NOV-2011	17:06:17.0	39.7921	-29.5926	4.9	11.0
22	21-NOV-2011	04:23:36.5	40.3413	-29.3722	3.3	14.0
23	22-NOV-2011	08:44:52.8	37.6739	-21.9466	4.2	10.0
24	26-NOV-2011	08:11:59.2	42.3437	-8.2945	4.0	26.8
25*	06-DEC-2011	19:12:07.0	36.8978	-12.9520	5.1	10.0
26	08-DEC-2011	08:54:45.1	38.0646	-30.7819	5.1	3.8
27	22-DEC-2011	06:07:21.4	37.1265	-24.3877	4.0	8.5
28	26-DEC-2011	04:33:54.7	31.3913	-7.3194	3.9	10.0
29	02-JAN-2012	19:47:35.1	36.1056	-7.4098	3.7	30.0
30	19-JAN-2012	14:03:27.1	32.5098	-7.5968	3.9	20.0
31*	23-JAN-2012	19:19:32.0	36.2957	-9.6290	4.8	10
32	18-FEB-2012	00:28:25.4	34.3852	-5.5433	4.6	10.0
33	28-FEB-2012	06:26:26.4	32.0222	-6.9073	3.8	10.0
34	02-MAR-2012	02:05:33.6	31.0326	-8.1654	3.9	5.0
35	09-MAR-2012	21:34:37.7	36.9104	-9.5801	2.6	30.0
36	10-MAR-2012	05:46:13.6	37.3329	-15.8607	3.5	10.0
37	12-MAR-2012	03:27:20.6	36.7307	-7.4766	4.0	30.0
38	13-MAR-2012	04:05:28.6	34.9282	-16.4454	4.5	30.0

cluster corresponds to events which occurred during a volcano eruption on the Canary Islands about 500 km south of Madeira.

5.2 DOCTAR array location results

Fig. 12 shows the DOCTAR location results. We used a distance of 200 km (i.e. 6 times the DOCTAR array radius) as the lower distance limit for the application of the plane-wave approach, that is events at larger distances were located with the plane-wave approach. For distances below 100 km, use of the plane-wave approach leads to severe bias due to effects of wavefront curvature (Bonney-Claudet *et al.* 2005) and in this distance range only the backprojection approach was used. For the distance range 100–200 km we mainly used also the backprojection approach, however, there are a few events where the P_o amplitude is so small that the backprojection approach misses P_o . In such cases the plane wavefront approach still lead to usable results. Events located with the plane wavefront approach are marked in lightgrey colour in Fig. 12, events located with the backprojection approach are marked in darkgrey colour.

Most events concentrate near the plate boundary and, as mentioned above, only few events at distances larger than 800 km could be located. In the east (between 16°W and 9°W longitude and at latitude 36°N) the distribution of epicentres deviates remarkably from the plate boundary given in the plate model published by Bird (2003, black line in Fig. 12). West of Madeira a cluster of earthquakes is located where only the largest two are found in the catalogue. Between the plate boundary and Madeira and only in the eastern oceanic part of the African Plate several earthquakes are located without obvious clustering. North of the plate boundary again distributed seismicity is found in the eastern oceanic part of the Eurasian Plate, while only a small number of events is found in the western oceanic part of the plate and on the mid-ocean ridge.

To better constrain the cluster west of Madeira we tried to use in addition to the OBS array's S_o backazimuths and P_o , S_o arrival times, the arrival times measured at other stations including regional permanent stations. We used the HYPOSAT software (Schweitzer 2001) to locate the events. For 7 events onsets could be picked on the traces of at least one Madeira array station. Out of the 7 events

Table 2. Velocity models for/near the DOCTAR array area. The ranges given in column 1 of Batista *et al.* (2017) denote layer thickness variations in the 2-D model, the ranges given in column 2 and 3 for the wave velocities correspond to values at top and base of the layer.

Thickness [km]	v_p [km s ⁻¹]	v_s [km s ⁻¹]
CRUST1.1 at 38.36°N, 18.37°W		
0.1	1.75	0.34
0.7	5.00	2.70
1.53	6.50	3.70
4.71	7.10	4.05
–	8.12	4.51
(Hannemann <i>et al.</i> 2016), Table 7 median model		
0.7±0.3	–	1.2±0.3
4.8±0.7	–	3.8±0.3
–	–	5.05±0.4
(Batista <i>et al.</i> 2017)		
0.5–0.7	1.8–3.4	1.0–1.9
1.0–3.2	4.5–5.8	2.4–3.3
5–5.5	6.2–7.0	3.5–3.75
4.0	7.1–7.4	3.75–3.9
–	7.8	4.5

Table 3. Station and phase specific amplitude correction terms used in the magnitude calculation. For *So* amplitudes 58 observations were used, while for *Po* only 19 recordings had a signal-to-noise ratio ≥ 3 at all stations.

Station	<i>Po</i>	<i>So</i>
D01	0.58±0.17	0.87±0.24
D02	1.16±0.27	1.13±0.27
D03	1.20±0.35	1.20±0.23
D04	0.95±0.24	0.81±0.15
D06	0.82±0.36	0.71±0.25
D07	1.00±0.23	1.00±0.21
D08	1.22±0.42	1.30±0.44
D09	0.89±0.29	0.76±0.27
D10	1.59±0.46	1.52±0.33
D11	0.50±0.20	0.44±0.17
D12	1.10±0.41	1.25±0.41

Table 4. Phase onsets detected at the different arrays between 4 July 2011 and 12 April 2012.

Array	Phases		
OBS	<i>Po</i>	<i>So</i>	
	323	1554	
Madeira	<i>Po</i>	<i>So</i>	
	93	171	
Evora	<i>Pn</i>	<i>Sn</i>	
	905	2055	
Evora	<i>Pg</i>	<i>Sg</i>	<i>Rg</i>
	1310	4370	861

which are located by the OBS array west of Madeira only one weak *P*-wave arrival can be associated with the event on 5 December 2011 01:40:15 at the Azores Island station CMLA. Open black thick line circles indicate the new locations in Fig. 12. On average the events change the estimated positions by 47 km, 2 events shift by up to 76 km, mostly towards northeastern direction, compared to the OBS array locations. Table 5 gives the locations of all events located with the plane-wave approach (most of them with a distance

larger than 200 km from station D01) where we set the hypocentre depth arbitrarily to 30 km. The location and origin time errors are calculated using the average backazimuth deviation of 5°, the standard deviation of the distance estimation error and the standard deviation of the origin time error obtained for the reference events. The locations of all events located with the backprojection approach are presented in Table 6 (mainly distances below 100 km). The error values in Table 6 for events located with the backprojection approach have to be considered as relative values. They were obtained by following the isoline marked by a 0.05 decrease in the semblance contour around the latitude, longitude, depth, origin time values for the semblance maximum. As expected especially the depth and the origin time parameter are coupled and show large errors for events at distances larger than one to two array apertures. The results from the backprojection approach for events near to the array are shown in a zoomed view in Fig. 13. The epicentres in Fig. 13(a) follow the proposed plate boundary between about 18°W and 16°W. From 19°W to 18°W only very small magnitude earthquakes are located. West of 19°W the earthquakes follow first an azimuth of about 290° up to about 20°W where the azimuth changes to about 250°. The hypocentres are projected in longitude bins of 1° width in longitude along latitude in Fig. 13(b). The hypocentres between about 18°W and 16°W align almost on a vertical line and reach there depths up to 60 km. However depth errors also reach 10–20 km at this distance to the array (Table 6). Beneath the OBS array smaller earthquakes at shallower depths down to about 30 km are found. The seismicity west of 19°W is mainly found at depths between 30 and 50 km.

Fig. 14(a) shows a zoomed display of event locations in the direct vicinity of the DOCTAR array. In addition to the backprojection locations we located the events with clear onset readings by manually picking onsets where we use again the local CRUST1.1 velocity model (see Table 2). The found hypocentres are shown by open black circles and match the hypocentres of the backprojection processing well (for the event parameters see also Table 7). No detailed structure is resolved within the array aperture. The inset in Fig. 14(a) shows two focal mechanisms for two events with an azimuthal gap of less than 80° (27 October 2011 21:32:46.2 and 10 April 2012 09:28:07.4). We used only *P*-wave polarities here because waveforms and *S*-wave amplitudes are strongly influenced by shallow sediments leading to reverberations and frequency dependent amplification. For the analysis the FOCMEC software was used (Snok *et al.* 1984). Two further (smaller magnitude) events at almost the same locations as the event of 27 October 2011 display the same polarity distribution at six stations with good signal-to-noise ratio. The focal mechanisms are not well constrained but show strike-slip characteristics consistent with right-lateral motion along an east–west oriented plane. Fig. 14(b) shows that most of the found earthquakes cluster in the northern part of the OBS array in a depth range down to about 30 km.

In Fig. 14(c) we display for the events located within the array the *S*-wave difference arrival times versus *P*-wave difference arrival times (manually picked arrivals). In that way we can determine the average v_p/v_s ratio by forming

$$\left(\frac{v_p}{v_s}\right)^{avg} = \sum_{i=1}^N \frac{t_{ij}^S - t_{ref,j}^S}{t_{ij}^P - t_{ref,j}^P}, \quad (5)$$

where t_{ij}^S , t_{ij}^P are *S*- and *P*-wave arrival times for event *j* at station *i* and $t_{ref,j}^S$, $t_{ref,j}^P$ are *S*- and *P*-wave arrival times for event *j* at a reference station (D01). The regression line in Fig. 14(c) has the slope $v_p/v_s^{avg} = 1.664 \pm 0.014$ and a constant of 0.219 ± 0.039 .

Table 5. Locations of events using plane-wave approach and DOCTAR array. δlat , δlon , δz and δt_0 denote epicentre and origin time errors calculated from a backazimuth error of 5° and standard deviations for event distance and origin time from reference events. The event depth is fixed.

Origin time	Lat. [$^\circ\text{N}$]	Lon. [$^\circ\text{E}$]	Depth [km]	M_L	δlat [$^\circ$]	δlon [$^\circ$]	δz [km]	δt_0 [s]
04-JUL-2011 12:30:01.296	38.615	-22.667	30.0	2.1	0.050	0.593	–	2.1
06-JUL-2011 10:51:51.458	37.004	-13.977	30.0	3.1	0.187	0.590	–	2.1
07-JUL-2011 00:48:36.930	39.029	-13.874	30.0	1.7	0.111	0.608	–	2.1
07-JUL-2011 20:05:55.300	34.007	-18.164	30.0	2.4	0.598	0.027	–	2.1
09-JUL-2011 13:54:50.995	36.846	-23.481	30.0	2.3	0.194	0.653	–	2.1
09-JUL-2011 14:08:30.759	37.452	-21.446	30.0	1.7	0.150	0.475	–	2.1
10-JUL-2011 09:38:27.648	36.924	-23.626	30.0	3.3	0.181	0.668	–	2.1
13-JUL-2011 00:34:29.265	36.818	-13.585	30.0	2.2	0.204	0.623	–	2.1
13-JUL-2011 19:41:35.520	36.732	-11.198	30.0	2.9	0.176	0.840	–	2.1
14-JUL-2011 15:00:06.914	36.676	-23.815	30.0	2.7	0.210	0.681	–	2.1
15-JUL-2011 03:11:17.097	37.604	-20.397	30.0	1.1	0.157	0.375	–	2.1
18-JUL-2011 09:28:15.625	37.225	-22.292	30.0	2.3	0.165	0.549	–	2.1
20-JUL-2011 18:04:54.959	40.516	-16.152	30.0	1.4	0.362	0.329	–	2.1
22-JUL-2011 15:06:09.036	37.171	-21.277	30.0	2.5	0.199	0.449	–	2.1
22-JUL-2011 19:19:28.689	36.374	-9.382	30.0	3.9	0.192	0.999	–	2.1
25-JUL-2011 02:12:58.555	38.283	-20.803	30.0	1.1	0.011	0.431	–	2.1
25-JUL-2011 02:12:57.987	37.857	-20.746	30.0	1.1	0.097	0.419	–	2.1
25-JUL-2011 18:31:21.391	39.015	-10.290	30.0	2.7	0.113	0.923	–	2.1
25-JUL-2011 19:18:29.185	37.217	-11.693	30.0	2.5	0.122	0.799	–	2.1
26-JUL-2011 11:12:26.524	37.076	-23.603	30.0	1.9	0.162	0.668	–	2.1
29-JUL-2011 03:20:39.931	36.591	-14.744	30.0	2.4	0.261	0.506	–	2.1
29-JUL-2011 09:25:25.675	37.930	-24.736	30.0	2.1	0.034	0.775	–	2.1
01-AUG-2011 23:06:18.521	33.376	-20.930	30.0	2.1	0.633	0.309	–	2.1
03-AUG-2011 00:21:38.214	37.686	-15.447	30.0	1.2	0.115	0.467	–	2.1
04-AUG-2011 04:36:53.066	37.453	-13.985	30.0	2.2	0.123	0.597	–	2.1
04-AUG-2011 07:31:39.858	33.217	-21.454	30.0	2.6	0.640	0.367	–	2.1
04-AUG-2011 15:16:51.396	30.057	-39.251	30.0	5.8	0.792	2.480	–	14.5
04-AUG-2011 23:33:10.209	37.273	-14.390	30.0	2.3	0.157	0.557	–	2.1
05-AUG-2011 04:25:11.086	37.441	-14.381	30.0	2.3	0.132	0.560	–	2.1
07-AUG-2011 10:53:57.934	36.281	-21.470	30.0	2.1	0.317	0.440	–	2.1
08-AUG-2011 12:39:12.857	37.527	-23.035	30.0	1.9	0.108	0.622	–	2.1
08-AUG-2011 19:44:06.360	37.484	-10.769	30.0	3.0	0.078	0.882	–	2.1
11-AUG-2011 11:57:01.104	37.379	-9.608	30.0	3.1	0.078	0.984	–	2.1
14-AUG-2011 16:53:55.987	37.226	-13.857	30.0	2.1	0.153	0.605	–	2.1
15-AUG-2011 03:23:05.119	37.499	-15.676	30.0	1.8	0.152	0.440	–	2.1
18-AUG-2011 05:37:47.567	37.855	-24.688	30.0	3.0	0.045	0.770	–	2.1
20-AUG-2011 03:27:15.785	35.712	-9.536	30.0	3.2	0.270	0.980	–	2.1
20-AUG-2011 13:03:26.072	38.341	-26.169	30.0	3.6	0.029	0.900	–	2.1
21-AUG-2011 09:00:10.722	36.331	-14.020	30.0	3.0	0.277	0.572	–	2.1
21-AUG-2011 11:39:48.555	38.196	-25.174	30.0	2.2	0.004	0.813	–	2.1
24-AUG-2011 09:48:50.521	34.445	-16.917	30.0	1.9	0.550	0.191	–	2.1
24-AUG-2011 16:53:25.329	35.912	-18.206	30.0	2.2	0.432	0.027	–	2.1
27-AUG-2011 07:35:36.785	37.203	-22.135	30.0	1.9	0.172	0.534	–	2.1
28-AUG-2011 03:53:02.615	36.721	-15.646	30.0	2.0	0.271	0.414	–	2.1
31-AUG-2011 12:17:14.838	43.530	-29.889	30.0	4.2	0.896	1.585	–	14.5
02-SEP-2011 02:47:10.338	38.558	-25.435	30.0	2.3	0.051	0.835	–	2.1
02-SEP-2011 05:26:17.759	37.581	-8.839	30.0	3.0	0.046	1.051	–	2.1
04-SEP-2011 07:00:29.853	38.042	-17.144	30.0	1.3	0.096	0.316	–	2.1
05-SEP-2011 08:33:04.295	38.000	-16.511	30.0	0.9	0.081	0.376	–	2.1
11-SEP-2011 08:28:42.568	33.298	-19.926	30.0	2.3	0.652	0.190	–	2.1
13-SEP-2011 14:04:02.791	37.646	-22.129	30.0	1.7	0.105	0.542	–	2.1
14-SEP-2011 00:42:50.060	41.156	-15.842	30.0	2.0	0.427	0.344	–	2.1
14-SEP-2011 19:22:59.085	37.132	-23.661	30.0	2.5	0.153	0.674	–	2.1
18-SEP-2011 08:26:47.833	37.927	-13.613	30.0	3.1	0.050	0.634	–	2.1
19-SEP-2011 08:12:31.522	38.050	-17.133	30.0	0.9	0.093	0.317	–	2.1
19-SEP-2011 19:54:04.436	41.089	-17.439	30.0	1.3	0.450	0.136	–	2.1
19-SEP-2011 19:55:40.944	39.833	-14.078	30.0	1.9	0.228	0.574	–	2.1
22-SEP-2011 03:43:30.243	37.056	-21.954	30.0	1.6	0.198	0.513	–	2.1
27-SEP-2011 04:56:19.663	33.737	-15.914	30.0	2.6	0.601	0.304	–	2.1
27-SEP-2011 12:29:58.087	37.857	-16.962	30.0	1.1	0.133	0.323	–	2.1
27-SEP-2011 14:47:26.553	22.818	-13.596	30.0	5.2	2.020	0.616	–	14.5
29-SEP-2011 07:55:28.994	43.721	-24.139	30.0	2.7	0.654	0.636	–	2.1
01-OCT-2011 00:10:25.415	36.190	-17.714	30.0	1.4	0.402	0.110	–	2.1

Table 5. Continued

Origin time	Lat. [°N]	Lon. [°E]	Depth [km]	M_L	δlat [°]	δlon [°]	δz [km]	δt_0 [s]
07-OCT-2011 22:18:27.846	38.431	-26.398	30.0	3.3	0.042	0.920	-	2.1
10-OCT-2011 01:16:23.018	43.631	-24.294	30.0	2.9	0.644	0.653	-	2.1
11-OCT-2011 07:59:05.612	37.067	-23.097	30.0	2.6	0.172	0.621	-	2.1
14-OCT-2011 05:42:43.504	37.692	-23.735	30.0	1.8	0.076	0.686	-	2.1
19-OCT-2011 08:00:18.968	37.758	-20.626	30.0	1.3	0.120	0.405	-	2.1
19-OCT-2011 17:12:54.703	36.905	-23.554	30.0	2.4	0.185	0.661	-	2.1
28-OCT-2011 17:03:52.090	37.275	-22.171	30.0	2.1	0.160	0.539	-	2.1
31-OCT-2011 20:12:21.072	36.860	-10.531	30.0	3.2	0.151	0.900	-	2.1
03-NOV-2011 05:53:20.638	43.835	-24.010	30.0	3.0	0.666	0.621	-	2.1
03-NOV-2011 14:54:12.062	37.537	-15.686	30.0	2.4	0.146	0.440	-	2.1
03-NOV-2011 17:37:25.696	36.706	-15.817	30.0	2.7	0.279	0.395	-	2.1
04-NOV-2011 01:47:27.923	37.593	-17.230	30.0	1.3	0.208	0.267	-	2.1
05-NOV-2011 12:47:27.040	36.846	-10.815	30.0	3.0	0.157	0.875	-	2.1
05-NOV-2011 13:54:05.306	37.024	-24.243	30.0	3.6	0.158	0.725	-	2.1
05-NOV-2011 14:27:20.009	37.147	-23.575	30.0	2.9	0.153	0.666	-	2.1
05-NOV-2011 20:54:44.696	37.309	-23.414	30.0	2.5	0.133	0.654	-	2.1
06-NOV-2011 05:45:23.828	37.039	-5.905	30.0	3.9	0.104	1.789	-	14.5
08-NOV-2011 22:06:01.588	36.830	-11.068	30.0	3.1	0.162	0.852	-	2.1
09-NOV-2011 04:06:07.956	36.733	-24.132	30.0	2.9	0.198	0.711	-	2.1
10-NOV-2011 08:25:03.084	34.939	-18.324	30.0	2.9	0.517	0.007	-	2.1
10-NOV-2011 11:56:34.145	37.354	-14.725	30.0	2.0	0.152	0.527	-	2.1
10-NOV-2011 23:31:59.025	37.761	-26.274	30.0	2.8	0.041	0.909	-	2.1
12-NOV-2011 13:11:18.048	37.592	-16.057	30.0	1.7	0.148	0.405	-	2.1
14-NOV-2011 02:02:45.774	37.256	-23.609	30.0	3.4	0.137	0.670	-	2.1
20-NOV-2011 14:31:01.048	32.047	-19.886	30.0	4.2	0.764	0.175	-	2.1
22-NOV-2011 21:19:01.544	33.976	-21.937	30.0	2.5	0.559	0.434	-	2.1
24-NOV-2011 12:12:52.883	37.810	-23.872	30.0	1.9	0.059	0.698	-	2.1
24-NOV-2011 20:04:55.107	37.588	-14.402	30.0	2.0	0.110	0.561	-	2.1
26-NOV-2011 08:12:24.359	41.612	-9.837	30.0	3.1	0.417	0.937	-	2.1
29-NOV-2011 16:10:01.577	35.300	-14.618	30.0	2.3	0.415	0.484	-	2.1
01-DEC-2011 07:30:14.988	41.797	-14.031	30.0	2.2	0.467	0.528	-	2.1
01-DEC-2011 15:07:15.713	36.729	-15.218	30.0	3.2	0.256	0.461	-	2.1
05-DEC-2011 01:40:09.291	33.074	-19.508	30.0	3.2	0.676	0.138	-	2.1
06-DEC-2011 19:12:06.337	37.024	-12.707	30.0	3.8	0.162	0.707	-	2.1
14-DEC-2011 17:51:45.055	33.787	-21.399	30.0	2.5	0.587	0.370	-	2.1
15-DEC-2011 09:10:48.142	43.325	-29.235	30.0	3.4	0.875	1.527	-	14.5
18-DEC-2011 17:01:11.593	36.801	-24.087	30.0	2.3	0.190	0.708	-	2.1
19-DEC-2011 03:50:51.204	37.745	-16.491	30.0	1.6	0.135	0.367	-	2.1
19-DEC-2011 18:15:38.968	37.645	-22.733	30.0	2.6	0.096	0.596	-	2.1
20-DEC-2011 06:07:54.039	39.274	-16.283	30.0	1.2	0.190	0.373	-	2.1
21-DEC-2011 23:25:11.919	36.994	-9.227	30.0	2.8	0.119	1.016	-	2.1
22-DEC-2011 00:31:42.538	38.152	-21.657	30.0	1.3	0.029	0.505	-	2.1
22-DEC-2011 06:07:17.597	36.832	-24.318	30.0	4.0	0.182	0.730	-	2.1
22-DEC-2011 18:25:56.962	34.999	-12.017	30.0	3.0	0.393	0.742	-	2.1
28-DEC-2011 06:59:15.521	44.393	-24.564	30.0	3.4	0.718	0.668	-	2.1
28-DEC-2011 13:29:10.776	35.543	-17.645	30.0	1.4	0.460	0.109	-	2.1
30-DEC-2011 06:50:49.021	37.873	-17.086	30.0	0.9	0.137	0.310	-	2.1
01-JAN-2012 10:10:56.188	37.828	-16.487	30.0	0.9	0.118	0.372	-	2.1
03-JAN-2012 14:46:41.186	38.099	-26.278	30.0	2.9	0.000	0.909	-	2.1
05-JAN-2012 15:49:24.952	44.304	-24.604	30.0	3.2	0.709	0.674	-	2.1
06-JAN-2012 15:20:20.460	37.511	-16.255	30.0	1.4	0.170	0.381	-	2.1
07-JAN-2012 23:51:01.265	37.661	-14.615	30.0	1.8	0.103	0.543	-	2.1
10-JAN-2012 02:53:20.241	38.056	-25.171	30.0	2.5	0.014	0.813	-	2.1
10-JAN-2012 10:55:55.798	37.225	-23.510	30.0	3.1	0.143	0.661	-	2.1
11-JAN-2012 07:43:36.383	33.965	-14.301	30.0	2.7	0.550	0.490	-	2.1
13-JAN-2012 15:14:50.578	35.122	-17.641	30.0	2.1	0.497	0.104	-	2.1
16-JAN-2012 19:44:43.814	36.075	-19.627	30.0	1.7	0.399	0.198	-	2.1
18-JAN-2012 05:25:31.544	39.319	-13.450	30.0	2.2	0.151	0.641	-	2.1
18-JAN-2012 09:47:42.274	33.185	-19.166	30.0	2.5	0.668	0.097	-	2.1
19-JAN-2012 00:11:34.617	39.230	-13.029	30.0	2.2	0.137	0.680	-	2.1
20-JAN-2012 02:15:36.639	38.312	-14.700	30.0	1.8	0.001	0.540	-	2.1
20-JAN-2012 15:57:11.534	37.507	-14.140	30.0	2.7	0.118	0.583	-	2.1
22-JAN-2012 19:09:39.722	38.327	-22.083	30.0	1.6	0.003	0.543	-	2.1
24-JAN-2012 15:14:24.667	33.026	-20.704	30.0	2.7	0.668	0.279	-	2.1
25-JAN-2012 05:00:47.586	35.341	-14.474	30.0	2.4	0.407	0.501	-	2.1

Table 5. Continued

Origin time	Lat. [°N]	Lon.[°E]	Depth [km]	M_L	δlat [°]	δlon [°]	δz [km]	δt_0 [s]
26-JAN-2012 22:42:19.105	38.115	-14.503	30.0	1.5	0.030	0.557	–	2.1
27-JAN-2012 04:59:42.703	44.168	-24.877	30.0	3.2	0.694	0.703	–	2.1
30-JAN-2012 02:09:20.556	32.791	-19.696	30.0	2.6	0.699	0.158	–	2.1
30-JAN-2012 05:27:28.739	37.312	-14.439	30.0	2.0	0.152	0.553	–	2.1
02-FEB-2012 11:40:53.435	32.731	-17.814	30.0	2.5	0.709	0.067	–	2.1
04-FEB-2012 15:55:59.114	36.436	-23.627	30.0	2.1	0.244	0.660	–	2.1
09-FEB-2012 08:01:45.203	37.772	-10.057	30.0	2.7	0.036	0.945	–	2.1
14-FEB-2012 09:34:19.051	37.516	-15.825	30.0	2.1	0.154	0.426	–	2.1
17-FEB-2012 00:14:54.067	35.283	-14.961	30.0	2.6	0.426	0.446	–	2.1
18-FEB-2012 00:28:50.318	36.160	-5.756	30.0	4.0	0.237	1.796	–	14.5
21-FEB-2012 21:20:11.439	37.811	-14.323	30.0	1.7	0.075	0.571	–	2.1
21-FEB-2012 22:16:19.192	38.247	-25.280	30.0	2.2	0.011	0.822	–	2.1
22-FEB-2012 18:55:50.779	37.432	-19.343	30.0	0.8	0.250	0.224	–	2.1
25-FEB-2012 05:20:10.571	35.634	-17.625	30.0	2.5	0.451	0.113	–	2.1
25-FEB-2012 07:35:51.307	33.566	-21.272	30.0	2.9	0.610	0.352	–	2.1
27-FEB-2012 10:14:15.945	37.576	-13.052	30.0	2.0	0.093	0.682	–	2.1
03-MAR-2012 06:30:09.673	38.283	-26.280	30.0	3.1	0.023	0.909	–	2.1
04-MAR-2012 12:00:50.735	36.143	-14.675	30.0	2.2	0.317	0.500	–	2.1
08-MAR-2012 02:53:08.556	36.967	-11.005	30.0	2.9	0.144	0.859	–	2.1
08-MAR-2012 08:03:38.026	36.888	-23.479	30.0	2.7	0.189	0.654	–	2.1
10-MAR-2012 05:32:33.564	37.582	-16.410	30.0	1.4	0.164	0.368	–	2.1
11-MAR-2012 14:06:51.089	34.642	-16.408	30.0	2.1	0.523	0.259	–	2.1
11-MAR-2012 17:10:40.685	37.601	-15.782	30.0	1.9	0.138	0.433	–	2.1
12-MAR-2012 12:10:13.781	36.964	-24.370	30.0	3.9	0.164	0.736	–	2.1
13-MAR-2012 04:05:31.623	34.945	-16.612	30.0	3.5	0.498	0.239	–	2.1
14-MAR-2012 01:28:32.256	37.902	-17.048	30.0	1.0	0.127	0.317	–	2.1
16-MAR-2012 06:35:37.630	42.814	-20.566	30.0	2.9	0.596	0.265	–	2.1
17-MAR-2012 14:14:02.036	36.743	-10.673	30.0	2.8	0.167	0.887	–	2.1
18-MAR-2012 05:32:04.587	35.307	-14.311	30.0	2.3	0.407	0.517	–	2.1
18-MAR-2012 23:10:59.812	36.992	-24.332	30.0	3.7	0.161	0.733	–	2.1
25-MAR-2012 03:32:48.514	37.501	-13.061	30.0	2.2	0.103	0.680	–	2.1
27-MAR-2012 10:43:14.921	37.661	-14.533	30.0	1.3	0.101	0.550	–	2.1
28-MAR-2012 02:23:02.225	36.273	-21.785	30.0	2.1	0.309	0.473	–	2.1
30-MAR-2012 04:32:20.096	40.158	-15.199	30.0	2.5	0.292	0.452	–	2.1
01-APR-2012 21:24:27.567	37.679	-17.103	30.0	0.4	0.182	0.293	–	2.1
02-APR-2012 12:25:03.632	38.891	-26.376	30.0	2.3	0.098	0.916	–	2.1
03-APR-2012 06:53:40.300	43.036	-14.295	30.0	4.2	0.599	0.473	–	2.1
03-APR-2012 20:48:43.873	37.313	-18.215	30.0	0.5	0.309	0.040	–	2.1
04-APR-2012 07:09:03.656	42.093	-11.282	30.0	3.2	0.475	0.795	–	2.1
05-APR-2012 16:47:21.711	37.046	-13.294	30.0	2.3	0.168	0.654	–	2.1
11-APR-2012 22:08:00.272	37.204	-13.903	30.0	2.7	0.157	0.600	–	2.1
12-APR-2012 17:16:33.667	38.711	-14.995	30.0	1.9	0.067	0.512	–	2.1
13-APR-2012 03:44:22.632	38.252	-16.645	30.0	1.2	0.025	0.370	–	2.1
13-APR-2012 11:01:03.636	37.683	-9.581	30.0	2.9	0.042	0.987	–	2.1
16-APR-2012 00:49:08.738	33.146	-18.865	30.0	2.4	0.672	0.060	–	2.1
16-APR-2012 14:41:02.447	37.214	-19.237	30.0	1.5	0.288	0.188	–	2.1
16-APR-2012 19:07:22.038	33.483	-20.761	30.0	2.1	0.626	0.291	–	2.1
16-APR-2012 20:37:48.102	37.196	-19.055	30.0	0.9	0.300	0.151	–	2.1
18-APR-2012 12:29:49.903	37.462	-15.780	30.0	2.6	0.162	0.428	–	2.1
18-APR-2012 13:00:19.962	37.603	-15.802	30.0	2.1	0.138	0.431	–	2.1
18-APR-2012 14:01:54.661	37.568	-20.819	30.0	1.5	0.148	0.417	–	2.1
19-APR-2012 14:13:23.531	37.536	-15.514	30.0	1.4	0.142	0.457	–	2.1
19-APR-2012 17:32:26.680	37.217	-13.172	30.0	2.1	0.143	0.667	–	2.1
19-APR-2012 23:41:08.409	34.703	-16.033	30.0	2.8	0.510	0.307	–	2.1
20-APR-2012 10:31:02.000	37.727	-19.599	30.0	1.5	0.175	0.290	–	2.1

The average of v_p/v_s ratios calculated from Wadati diagrams for single well recorded local events is 1.65 ± 0.07 . This v_p/v_s ratio is low compared to standard models (i.e. v_p/v_s about 1.8 in the PREM model G15) and also lower than the v_p/v_s ratio of 1.85 of the uppermost 40 km of the local CRUST1.1 model G41 which was used for backprojection, location with manual picks and focal mechanism determination here.

6 DISCUSSION

6.1 Technical issues

We have shown that a mid-aperture array in the deep ocean can be successfully used to monitor regional seismicity in the oceanic lithosphere in a frequency range between 4 and 25 Hz. In order to overcome the alias problem for wavelengths much smaller than

Table 6. Locations of events using backprojection approach and DOCTAR array. Events beneath the DOCTAR array which were also located using traveltime picks (see Table 7) are marked with a star in the leftmost column. δlat , δlon , δz and δt_0 denote relative errors in hypocentre position and origin time calculated from a -0.05 decrease isocontour relative to the found semblance maximum.

Origin time	Lat. [°N]	Lon. [°E]	Depth [km]	M_L	δlat [°]	δlon [°]	δz [km]	δt_0 [s]
05-JUL-2011 22:16:26.220	37.750	-17.750	47.0	1.0	0.025	0.025	5.0	0.9
10-JUL-2011 02:36:00.220	38.550	-18.250	19.0	-0.5	0.000	0.150	4.0	6.9
11-JUL-2011 10:30:10.220	37.550	-16.600	41.0	1.3	0.125	0.100	23.0	2.2
13-JUL-2011 17:17:47.220	37.850	-18.650	19.0	0.6	0.025	0.025	3.0	0.7
14-JUL-2011 02:02:43.220	37.800	-18.300	13.0	0.4	0.025	0.000	6.0	0.7
14-JUL-2011 16:26:10.220	37.650	-17.750	45.0	0.8	0.050	0.050	9.0	0.9
18-JUL-2011 06:48:31.220	37.650	-17.400	49.0	2.1	0.050	0.050	10.0	0.9
23-JUL-2011 05:45:42.220	37.700	-17.350	31.0	1.7	0.025	0.050	12.0	0.9
23-JUL-2011 17:29:08.220	39.150	-19.300	65.0	1.9	0.100	0.125	12.0	1.2
24-JUL-2011 17:15:53.220	37.700	-17.400	1.0	0.8	0.050	0.050	6.0	0.9
25-JUL-2011 15:39:29.220	37.850	-19.350	41.0	1.4	0.025	0.075	8.0	1.2
03-AUG-2011 02:55:07.720	38.400	-18.400	1.0	-0.8	0.000	0.050	4.0	0.7
*03-AUG-2011 12:40:24.220	38.050	-18.600	69.0	1.1	0.050	0.075	6.0	0.9
05-AUG-2011 13:58:20.220	37.550	-16.750	63.0	2.4	0.050	0.050	10.0	0.9
06-AUG-2011 12:57:25.220	37.700	-16.850	51.0	1.7	0.050	0.050	8.0	0.7
06-AUG-2011 20:02:33.220	37.850	-18.900	27.0	1.2	0.025	0.025	7.0	0.9
08-AUG-2011 09:36:56.720	37.800	-18.050	33.0	1.3	0.025	0.000	5.0	0.7
12-AUG-2011 09:32:15.720	40.150	-16.800	1.0	2.5	0.050	0.100	34.0	1.2
*14-AUG-2011 19:31:39.220	38.300	-18.200	25.0	1.0	0.000	0.000	3.0	0.7
15-AUG-2011 10:30:05.220	37.650	-17.450	49.0	1.7	0.025	0.050	6.0	0.7
16-AUG-2011 11:32:19.220	37.550	-17.450	53.0	0.9	0.075	0.075	8.0	1.2
17-AUG-2011 11:56:34.220	37.900	-19.700	3.0	1.0	0.075	0.050	23.0	1.2
19-AUG-2011 09:02:16.720	37.250	-16.300	23.0	2.6	0.075	0.050	29.0	1.2
20-AUG-2011 03:34:05.720	37.700	-17.600	59.0	0.8	0.050	0.050	6.0	0.9
20-AUG-2011 20:09:56.720	39.450	-18.450	23.0	0.9	0.050	0.000	17.0	0.9
21-AUG-2011 13:01:07.720	37.600	-16.750	61.0	2.0	0.100	0.050	14.0	1.2
21-AUG-2011 22:19:22.220	37.450	-20.300	39.0	2.1	0.075	0.075	19.0	1.2
22-AUG-2011 20:21:15.720	37.500	-18.850	13.0	1.5	0.050	0.075	19.0	1.2
23-AUG-2011 17:18:39.720	37.650	-18.700	29.0	0.6	0.025	0.050	10.0	0.7
24-AUG-2011 19:25:41.720	37.700	-18.500	23.0	0.8	0.050	0.025	7.0	0.7
25-AUG-2011 15:35:25.220	37.700	-16.450	61.0	2.1	0.100	0.050	14.0	1.2
26-AUG-2011 00:05:45.220	37.700	-17.600	53.0	1.1	0.050	0.050	12.0	1.5
*03-SEP-2011 00:20:16.720	37.600	-18.250	29.0	1.0	0.000	0.000	9.0	0.7
03-SEP-2011 16:52:31.720	38.600	-18.350	3.0	0.0	0.000	0.000	14.0	0.7
06-SEP-2011 01:38:03.220	37.250	-16.700	63.0	1.1	0.075	0.050	7.0	0.9
06-SEP-2011 13:02:34.720	37.850	-19.450	7.0	1.1	0.050	0.050	3.0	0.9
06-SEP-2011 14:09:50.720	37.850	-19.450	3.0	0.9	0.050	0.050	19.0	0.9
07-SEP-2011 00:53:43.220	37.750	-19.400	35.0	1.8	0.025	0.025	10.0	0.9
08-SEP-2011 12:56:53.720	37.550	-18.900	43.0	1.9	0.075	0.150	18.0	1.5
12-SEP-2011 12:21:41.220	37.650	-19.000	7.0	0.6	0.025	0.050	2.0	0.9
13-SEP-2011 19:54:38.220	37.700	-17.400	21.0	1.6	0.050	0.100	22.0	1.2
15-SEP-2011 20:20:06.220	37.700	-17.450	37.0	0.6	0.025	0.050	10.0	0.7
15-SEP-2011 21:03:56.720	39.000	-16.650	43.0	0.9	0.075	0.225	18.0	4.2
17-SEP-2011 17:38:41.220	38.050	-18.150	21.0	0.4	0.000	0.025	4.0	0.7
*19-SEP-2011 05:37:45.220	38.050	-18.150	29.0	2.1	0.000	0.000	3.0	0.7
21-SEP-2011 01:30:26.720	36.800	-18.350	69.0	2.7	0.025	0.025	8.0	0.9
*23-SEP-2011 02:30:14.220	38.550	-18.150	27.0	1.1	0.000	0.000	3.0	0.7
25-SEP-2011 17:29:09.720	37.650	-16.700	69.0	4.3	0.050	0.075	4.0	0.9
25-SEP-2011 18:06:52.720	38.250	-18.200	3.0	-0.2	0.000	0.050	1.0	1.2
25-SEP-2011 18:53:22.220	37.650	-16.600	13.0	1.0	0.100	0.075	25.0	1.2
25-SEP-2011 19:06:04.720	37.650	-16.700	55.0	1.5	0.050	0.050	19.0	1.2
25-SEP-2011 20:41:24.720	37.500	-16.750	7.0	0.9	0.075	0.050	28.0	1.2
25-SEP-2011 21:31:26.720	37.600	-16.750	63.0	2.5	0.075	0.050	8.0	0.9
26-SEP-2011 03:54:35.220	37.750	-16.450	7.0	1.7	0.075	0.075	7.0	1.2
26-SEP-2011 18:34:48.720	37.650	-16.800	67.0	1.7	0.075	0.050	9.0	1.2
29-SEP-2011 06:21:02.220	37.600	-19.000	35.0	2.2	0.025	0.075	7.0	0.9
29-SEP-2011 07:08:33.220	37.600	-19.050	27.0	1.9	0.025	0.050	10.0	0.9
30-SEP-2011 09:02:05.220	38.250	-18.200	1.0	-0.0	0.000	0.000	1.0	0.4
03-OCT-2011 05:39:02.720	37.900	-19.100	37.0	1.5	0.025	0.050	9.0	0.9
04-OCT-2011 07:35:59.720	37.850	-19.450	3.0	1.3	0.050	0.050	3.0	1.2
05-OCT-2011 03:18:19.720	37.750	-17.650	39.0	1.2	0.025	0.025	6.0	0.7
06-OCT-2011 14:57:26.720	37.650	-16.650	29.0	1.8	0.075	0.050	16.0	0.9

Table 6. Continued

Origin time	Lat. [°N]	Lon. [°E]	Depth [km]	M_L	δlat [°]	δlon [°]	δz [km]	δt_0 [s]
07-OCT-2011 13:15:09.720	37.650	-16.500	1.0	1.4	0.075	0.050	28.0	0.9
09-OCT-2011 20:48:57.720	37.650	-19.150	67.0	0.8	0.075	0.050	4.0	0.9
*11-OCT-2011 00:46:26.220	38.500	-18.350	5.0	-0.2	0.000	0.000	5.0	0.4
11-OCT-2011 03:02:18.220	37.750	-19.550	31.0	2.7	0.050	0.050	17.0	0.9
13-OCT-2011 21:06:25.720	37.750	-20.300	61.0	1.3	0.100	0.050	14.0	1.2
14-OCT-2011 17:48:15.720	37.400	-18.650	1.0	0.9	0.025	0.100	28.0	0.9
*14-OCT-2011 19:36:09.220	38.500	-18.300	29.0	0.7	0.000	0.000	3.0	0.7
17-OCT-2011 07:10:23.220	38.650	-17.600	17.0	1.4	0.025	0.025	9.0	0.7
17-OCT-2011 22:23:38.720	37.500	-20.500	69.0	2.1	0.125	0.100	8.0	1.5
18-OCT-2011 09:06:57.220	37.850	-18.900	15.0	0.5	0.050	0.050	16.0	1.2
25-OCT-2011 08:02:28.220	40.300	-18.150	3.0	2.2	0.050	0.125	27.0	1.2
*27-OCT-2011 12:41:11.220	38.050	-18.750	7.0	0.3	0.050	0.050	3.0	0.9
*27-OCT-2011 21:32:46.220	38.500	-18.300	33.0	1.6	0.000	0.025	3.0	0.9
29-OCT-2011 06:57:13.720	37.600	-16.500	41.0	1.3	0.075	0.050	21.0	1.2
30-OCT-2011 18:32:32.720	37.600	-18.300	35.0	0.8	0.050	0.000	7.0	0.7
30-OCT-2011 23:11:30.220	37.700	-17.750	41.0	1.4	0.050	0.050	12.0	1.2
06-NOV-2011 11:51:50.720	37.550	-17.150	65.0	1.9	0.050	0.075	12.0	0.9
10-NOV-2011 03:57:35.720	37.500	-18.850	35.0	1.6	0.025	0.025	11.0	0.9
12-NOV-2011 13:42:18.220	38.400	-18.000	1.0	0.8	0.000	0.025	0.0	0.7
19-NOV-2011 12:55:31.720	40.250	-17.200	69.0	2.5	0.050	0.075	10.0	1.2
19-NOV-2011 13:39:44.720	37.500	-16.900	5.0	1.4	0.050	0.050	4.0	0.7
20-NOV-2011 12:59:50.720	37.700	-19.100	27.0	1.1	0.025	0.050	9.0	0.7
20-NOV-2011 15:35:21.220	37.250	-16.350	15.0	2.4	0.100	0.075	13.0	1.2
20-NOV-2011 17:24:57.220	37.600	-17.350	43.0	1.1	0.100	0.075	18.0	1.5
23-NOV-2011 00:11:23.220	37.800	-19.900	49.0	1.3	0.075	0.050	17.0	1.2
25-NOV-2011 03:30:03.720	37.650	-17.700	5.0	0.6	0.025	0.075	3.0	0.9
27-NOV-2011 05:17:07.220	37.800	-19.850	39.0	3.6	0.050	0.050	15.0	0.9
29-NOV-2011 02:37:12.220	37.600	-19.100	9.0	0.6	0.125	0.075	4.0	0.9
*29-NOV-2011 22:42:41.220	38.800	-18.450	13.0	1.4	0.000	0.000	2.0	0.4
02-DEC-2011 19:33:23.720	37.400	-18.900	43.0	2.4	0.025	0.050	5.0	0.9
04-DEC-2011 16:49:37.220	37.800	-17.300	3.0	1.0	0.075	0.050	3.0	0.9
07-DEC-2011 22:11:35.220	37.900	-20.000	41.0	1.4	0.050	0.050	11.0	0.9
11-DEC-2011 01:05:26.220	37.900	-19.900	55.0	1.2	0.050	0.050	11.0	0.9
27-DEC-2011 04:25:12.220	37.650	-19.400	57.0	1.0	0.075	0.075	13.0	1.5
31-DEC-2011 00:41:32.720	37.750	-17.200	51.0	2.0	0.050	0.050	8.0	0.9
31-DEC-2011 23:46:08.720	37.450	-16.200	11.0	1.6	0.150	0.050	30.0	1.5
04-JAN-2012 21:11:48.220	37.750	-18.600	21.0	0.7	0.075	0.050	10.0	0.9
05-JAN-2012 05:35:45.720	37.400	-19.500	57.0	1.4	0.050	0.075	14.0	1.2
09-JAN-2012 11:44:02.220	37.650	-16.700	1.0	1.5	0.075	0.075	31.0	1.2
11-JAN-2012 08:46:35.720	37.950	-19.000	17.0	0.8	0.025	0.050	8.0	0.9
*11-JAN-2012 13:56:24.220	37.950	-18.900	5.0	0.8	0.025	0.025	3.0	0.7
11-JAN-2012 23:55:03.720	37.750	-17.400	47.0	1.7	0.050	0.050	8.0	0.9
12-JAN-2012 19:12:03.220	37.900	-20.050	67.0	1.3	0.075	0.050	11.0	1.2
13-JAN-2012 00:22:21.220	37.650	-17.700	45.0	0.9	0.025	0.050	4.0	0.7
13-JAN-2012 00:44:02.220	38.200	-18.650	1.0	-0.3	0.000	0.000	1.0	0.4
13-JAN-2012 10:13:02.220	37.700	-18.700	29.0	1.3	0.000	0.025	7.0	0.7
16-JAN-2012 14:29:54.720	37.450	-18.900	1.0	2.7	0.050	0.050	8.0	0.9
23-JAN-2012 03:16:51.720	37.800	-18.950	1.0	0.9	0.025	0.050	4.0	0.7
23-JAN-2012 13:05:47.720	37.700	-17.300	15.0	2.4	0.050	0.075	8.0	0.9
26-JAN-2012 20:30:45.220	39.200	-17.100	1.0	1.1	0.050	0.025	4.0	1.2
27-JAN-2012 10:23:23.720	37.950	-19.000	23.0	0.7	0.025	0.050	6.0	0.7
28-JAN-2012 05:46:02.220	37.700	-17.450	49.0	1.2	0.025	0.050	7.0	0.9
31-JAN-2012 14:14:03.720	37.750	-17.700	47.0	1.1	0.025	0.025	7.0	0.9
01-FEB-2012 14:57:30.720	38.400	-18.300	7.0	-0.6	0.025	0.000	0.0	0.4
02-FEB-2012 00:47:55.720	38.400	-18.300	21.0	0.1	0.000	0.025	9.0	1.5
02-FEB-2012 19:44:16.720	38.350	-18.750	1.0	-0.2	0.000	0.050	1.0	1.2
04-FEB-2012 01:35:23.220	37.650	-16.700	69.0	1.8	0.075	0.050	7.0	0.9
05-FEB-2012 20:23:12.220	37.550	-16.600	45.0	2.8	0.075	0.075	15.0	1.2
*08-FEB-2012 11:04:19.720	38.500	-18.050	1.0	0.4	0.075	0.050	9.0	0.9
12-FEB-2012 05:06:47.220	37.300	-20.850	5.0	1.6	0.100	0.050	7.0	1.2
16-FEB-2012 17:49:56.220	37.700	-17.500	49.0	2.0	0.050	0.050	7.0	0.9
16-FEB-2012 23:22:21.220	37.650	-19.150	69.0	2.0	0.125	0.125	5.0	2.0
17-FEB-2012 05:22:30.720	37.650	-17.450	45.0	2.4	0.050	0.025	8.0	0.9
18-FEB-2012 12:42:32.720	37.650	-17.600	11.0	1.3	0.025	0.075	6.0	1.2
21-FEB-2012 10:26:08.220	37.850	-18.750	61.0	0.9	0.050	0.075	7.0	1.2

Table 6. Continued

Origin time	Lat. [°N]	Lon. [°E]	Depth [km]	M_L	δlat [°]	δlon [°]	δz [km]	δt_0 [s]
21-FEB-2012 22:50:42.720	37.700	-20.400	45.0	1.4	0.075	0.050	23.0	0.9
22-FEB-2012 15:19:37.220	38.450	-16.850	39.0	1.2	0.000	0.075	19.0	1.2
23-FEB-2012 11:50:07.220	37.700	-16.700	51.0	1.3	0.075	0.025	13.0	0.9
23-FEB-2012 21:05:47.220	37.700	-17.450	41.0	1.1	0.025	0.050	18.0	1.5
23-FEB-2012 21:52:35.220	37.700	-17.800	7.0	0.6	0.050	0.050	7.0	1.2
23-FEB-2012 23:38:07.720	37.550	-18.550	49.0	1.3	0.050	0.000	7.0	0.9
24-FEB-2012 05:31:49.220	37.750	-17.750	63.0	1.6	0.100	0.125	10.0	1.5
24-FEB-2012 12:54:02.720	37.750	-17.250	57.0	1.3	0.025	0.050	8.0	1.2
25-FEB-2012 18:25:07.720	37.550	-16.700	1.0	2.1	0.050	0.050	26.0	1.2
26-FEB-2012 19:22:26.720	37.650	-18.750	19.0	1.2	0.025	0.025	9.0	0.7
27-FEB-2012 11:13:20.720	37.700	-17.450	57.0	1.7	0.050	0.075	7.0	0.9
28-FEB-2012 07:20:27.220	37.650	-17.450	43.0	1.7	0.050	0.050	9.0	0.9
01-MAR-2012 19:17:32.720	37.650	-17.450	47.0	1.1	0.050	0.050	12.0	1.2
02-MAR-2012 09:14:54.720	37.650	-20.200	47.0	2.5	0.100	0.075	16.0	1.5
04-MAR-2012 20:27:33.720	37.600	-19.350	27.0	0.8	0.050	0.050	11.0	0.9
07-MAR-2012 15:20:23.220	38.900	-17.150	25.0	2.0	0.025	0.025	22.0	0.9
07-MAR-2012 16:24:53.220	37.400	-18.750	17.0	0.6	0.050	0.050	20.0	0.9
07-MAR-2012 17:27:12.220	37.900	-19.450	31.0	2.3	0.025	0.025	9.0	0.7
*09-MAR-2012 19:25:55.220	38.500	-18.000	5.0	0.8	0.000	0.000	1.0	0.4
10-MAR-2012 05:46:16.220	37.600	-16.650	47.0	2.9	0.050	0.075	18.0	1.2
10-MAR-2012 10:48:18.720	37.450	-18.250	35.0	1.3	0.025	0.025	11.0	1.2
10-MAR-2012 15:36:16.720	37.900	-18.950	13.0	0.7	0.050	0.050	3.0	0.9
11-MAR-2012 19:55:28.220	38.450	-17.450	25.0	1.2	0.000	0.050	8.0	1.2
13-MAR-2012 06:18:23.220	37.750	-16.600	1.0	1.4	0.075	0.050	27.0	0.9
17-MAR-2012 23:40:40.720	37.600	-19.300	39.0	2.7	0.025	0.050	11.0	0.9
19-MAR-2012 02:21:21.220	37.700	-17.800	43.0	0.9	0.050	0.025	8.0	0.9
20-MAR-2012 17:09:19.220	37.750	-19.150	35.0	0.8	0.025	0.075	8.0	0.9
20-MAR-2012 19:55:53.720	37.600	-16.650	43.0	2.1	0.075	0.100	26.0	1.5
25-MAR-2012 03:26:04.720	37.700	-16.450	3.0	1.3	0.050	0.050	19.0	0.7
27-MAR-2012 02:10:09.720	38.100	-18.050	1.0	-0.1	0.000	0.175	3.0	0.9
27-MAR-2012 12:13:01.720	38.500	-18.250	21.0	-0.1	0.000	0.000	9.0	0.7
27-MAR-2012 18:57:51.220	37.950	-18.200	5.0	-0.2	0.025	0.025	15.0	0.9
28-MAR-2012 02:43:34.720	37.700	-17.800	7.0	1.9	0.025	0.050	3.0	0.7
29-MAR-2012 04:05:59.720	36.700	-17.650	1.0	1.0	0.025	0.125	33.0	0.9
*31-MAR-2012 04:09:43.720	38.400	-17.950	31.0	0.6	0.000	0.025	3.0	0.9
24-MAR-2012 10:21:05.720	37.550	-20.300	5.0	1.0	0.050	0.025	3.0	0.7
27-MAR-2012 12:05:53.220	37.650	-18.950	45.0	0.7	0.050	0.050	17.0	1.5
29-MAR-2012 02:50:58.720	38.050	-19.950	59.0	0.6	0.075	0.075	18.0	1.2
09-APR-2012 11:00:39.220	38.250	-18.200	5.0	-0.2	0.000	0.000	14.0	0.9
*10-APR-2012 09:28:07.720	38.400	-18.250	29.0	1.0	0.000	0.000	3.0	0.7
11-APR-2012 02:10:02.720	37.650	-17.450	17.0	1.0	0.025	0.075	9.0	0.9
11-APR-2012 18:28:31.720	37.700	-19.300	5.0	0.6	0.050	0.050	4.0	0.7
11-APR-2012 21:19:50.720	37.650	-16.650	67.0	1.8	0.100	0.050	17.0	1.2
12-APR-2012 14:05:24.220	37.650	-18.900	31.0	1.0	0.025	0.050	10.0	0.9

the interstation distances, we implemented an incoherent beamforming approach to create long-period pseudo-waveforms to determine plane-wave parameters and to locate events by amplitude migration (backprojection) for events located near to or beneath the array. To use waveform coherency directly to increase the signal-to-noise ratio in the beamforming process one would have to construct much smaller arrays (Schweitzer *et al.* 2012). However, it is still technically challenging to build such small aperture detection arrays in the deep ocean. A general problem is the exact station placing and location of free-fall stations, if apertures of a few hundred metres and interstation distances of tens of metres up to 100 m have to be realized to ensure coherent stacking of the high-frequency *Po* and *So* waveforms without spatial aliasing. Exploiting waveform coherency to decrease the monitoring threshold using the classical delay-and-sum beamforming array approach is to our knowledge not tested yet. Potentially a small-aperture deep ocean array could outperform a large aperture array

in terms of required ship-time, as the large aperture array outperforms the seismic network. In comparison the building and maintenance of the arrays on Madeira and near Evora were cheaper (maintenance was possible). However restrictions due to limited area (Madeira), high topography (Madeira) and lack of support of local landowners (Madeira, Evora) and interference with human infrastructure like traffic lines (Madeira, Evora) caused non-optimal array configurations.

6.2 Monitoring results

We have shown that the OBS array clearly outperformed the Madeira array in terms of monitoring thresholds and performed on an equal footing compared with the Evora array. Generally noise levels in the ocean were on average higher than in the other two environments. However observation conditions are in the deep ocean on average more steady and anthropogenic noise sources like ships are

Table 7. Locations of events beneath the DOCTAR array using the HYPOSAT software. δlat , δlon , δz and δt_0 denote errors in hypocentre position and origin time calculated from traveltime pick errors.

Origin time	Lat. [°N]	Lon. [°E]	Depth [km]	δlat [°]	δlon [°]	δz [km]	δt_0 [s]
22-JUL-2011 15:06:15.6	37.584	-21.011	51.98	0.0621	0.0794	34.75	0.412
03-AUG-2011 12 40 19.764	37.820	-18.697	0.10	0.0808	0.0444	3.03	0.662
14-AUG-2011 19 31 39.245	38.296	-18.174	24.95	0.0192	0.0095	1.32	0.164
03-SEP-2011 00 20 15.380	37.535	-18.301	25.77	0.0347	0.0488	17.08	0.339
19-SEP-2011 05 37 45.729	38.050	-18.148	27.52	0.0131	0.0158	2.05	0.173
23-SEP-2011 02 30 13.693	38.571	-18.137	30.95	0.0146	0.0158	1.68	0.184
11-OCT-2011 00 46 16.562	38.501	-18.293	33.33	0.0177	0.0210	2.23	0.335
14-OCT-2011 19 36 08.358	38.501	-18.281	34.02	0.0157	0.0197	1.81	0.297
27-OCT-2011 12 40 50.287	37.964	-19.329	28.78	0.0430	0.0868	13.93	0.447
27-OCT-2011 21 32 46.202	38.494	-18.287	32.44	0.0084	0.0119	1.32	0.157
29-NOV-2011 22 42 40.429	38.831	-18.449	14.75	0.0168	0.0141	3.76	0.214
11-JAN-2012 13 56 20.746	37.850	-19.045	16.21	0.0617	0.0684	26.46	0.596
08-FEB-2012 11 04 10.291	38.443	-18.030	27.54	0.0105	0.0082	1.04	0.148
09-MAR-2012 19 25 54.496	38.494	-18.003	0.10	0.0155	0.0225	0.81	0.185
31-MAR-2012 04 09 43.357	38.421	-17.954	31.37	0.0532	0.0362	4.16	0.519
10-APR-2012 09 28 07.405	38.407	-18.265	29.50	0.0098	0.0145	1.39	0.179

more rare in time and are more local in their nature. Compared to Madeira the topography in the OBS array is smoother while the aperture is larger. The better monitoring performance of DOCTAR compared to the Madeira Array can also be partially explained by the more homogeneous crust and mantle beneath the DOCTAR site (Matos *et al.* 2015; Hannemann *et al.* 2016). The Evora array detected the highest total number of seismic onsets. However, the number of tectonic events is much smaller than the total number of events. Fig. 15 shows all detections at the three arrays sorted by daytime. It is obvious that most events are observed during working hours at the Evora array (Fig. 15b), while there is no such daytime dependence visible in the OBS array detections (Fig. 15a). That makes an anthropogenic origin likely. Fig. 10 showed that the DOCTAR locations for selected well localized larger magnitude events agree well with catalogue locations up to distances of about 900 km. Here the Madeira array showed the least good results likely caused by its smaller aperture, elliptical array layout shape and the high topography/heterogeneity in the array. In terms of detection thresholds the Evora array could not detect the selected events in the oceanic plate at distances larger than about 800 km.

Fig. 16 shows the found magnitude/distance relationship for all events located with the DOCTAR array. We find a magnitude threshold of about $M_L = 2$ up to distances of 500 km. We conclude that a large aperture seismological array in the deep ocean can be used to monitor and locate the small and medium magnitude seismicity in the interior of an oceanic plate for up to 500 km if a magnitude threshold of $M_L = 2$, and up to 1000 km if a magnitude threshold of $M_L = 3$, is required.

6.3 Regional seismicity

We start the discussion of the seismicity in the West with the non-observation of *Po/So* wave trains from the Azores Islands. No events could be found west of 27°W (Fig. 12) where the Azores plateau is located (Silveira *et al.* 2010). During the observation period of the OBS array the strongest event with magnitude $M_w = 5.1$ occurred south of the Azores Islands and could be observed only weakly in longperiod filtered records. On the ridge segment to the North of the Azores we found *Po* onsets from three events with M_L about 4 but only weak to non-visible *So* onsets. Between 27°W and 22°W the events follow the Terceira Rift structure, where the observed events

correlate with locations of normal fault events (Custodio *et al.* 2016, see their fig. 6).

The Azores plateau has larger crustal thickness than the surrounding oceanic areas. While a gravity modeling study finds an average crustal thickness of about 10 km (Gente *et al.* 2003), a receiver function study gives higher values between 20 and 30 km below the eastern islands (Silveira *et al.* 2010). The same study finds a high velocity mantle lid with a low v_p/v_s ratio of about 1.65. Most local earthquakes on the Azores plateau occur in the crust and because the crust is of lower velocity than the oceanic mantle it might be difficult to transmit high-frequency wavefield energy to the oceanic mantle to form *Po/So* wave trains. The high velocity, low v_p/v_s ratio mantle lid below the crust is suspected to be caused by high depletion of the mantle or a different mineralogical composition (Silveira *et al.* 2010). It is therefore possible that high velocity frozen melt lenses assumed to cause whispering gallery *Po/So* waves (Kennett & Furumura 2013) are not existing beneath the Azores plateau. Finally several studies (e.g. Pilidou *et al.* 2004; Silveira *et al.* 2006) imaged with surface waves a pronounced low velocity structure in the upper mantle below the Azores plateau forming the root of the active volcanism on several of the islands. It is well-known from other volcanic regions, that volcanism is often related to strong attenuation of seismic waves in the lithosphere and this effect was recently also observed for *Po/So* waves (Kennett & Furumura 2015).

Fig. 13 displays the seismic events found to the South of the OBS array. Larger magnitude events up to magnitude 4 are only found in southwestern and southeastern direction, while only small magnitude events are found between longitude 18.9°W and 17.8°W. This seismic gap coincides well with the location of the 25 November 1941 M8.3 event located by jointly inverting historical seismograms and tsunami recordings (Baptista *et al.* 2016). The length of the rupture is given as 160 km in Baptista *et al.* (2016) almost reaching 20°W, where we map a WNW–ESE striking structure with earthquakes up to magnitude about 3 between about 19°W and 19.9°W (see Fig. 13a for details). Directly to the west of the gap in seismicity it is remarkable that the stronger events are limited rather sharply to hypocentre depths ≥ 20 km (see grey dashed line in Fig. 13b). This feature possibly indicates the presence of a serpentized layer in the uppermost mantle and crust as was observed in a seismic line across the Gloria fault about 200 km to the West (Batista *et al.* 2017). However, given the hypocentre depth uncertainties (see Table 6), it remains speculative to connect a possible transition from

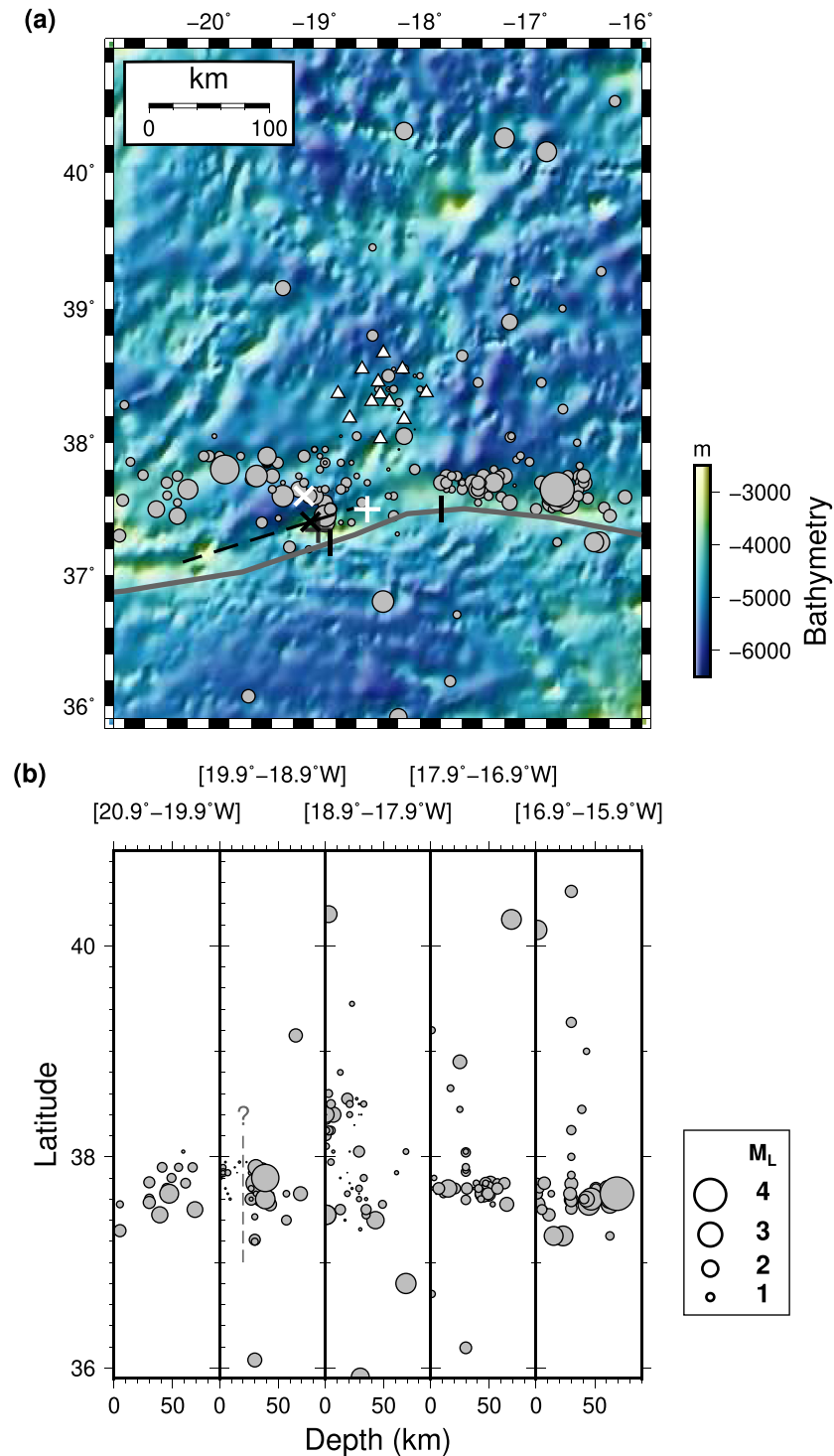


Figure 13. (a) Event epicentres localized by the OBS array at near regional distance using the backprojection approach. White triangles mark the position of the DOCTAR stations, grey circles mark the events. The white plus marks the epicentre for the 1941 Gloria fault earthquake published by Gutenberg & Richter (1949), the white cross marks the epicentre given by Lynnes & Ruff (1985), the dark grey plus marks the epicentre by Baptista *et al.* (2016) using the IASP91 velocity model and the black cross and the black dashed line mark the epicentre and rupture extension by Baptista *et al.* (2016) using the regional velocity model by Carrilho *et al.* (2004). Black bars mark the seismic gap south of DOCTAR. (b) Hypocentres plotted in 1° wide bins in longitude (as marked on top of the respective areas) as function of depth and latitude). The dashed grey line marks a potential upper depth boundary for seismic events.

an unserpentinized region to a serpentinized one with the stop of the rupture of the 1941 event.

The seismic events in the southeast (east of 17.8°W) align on an almost vertical fault plane. To the southwest (west of 18.9°W)

the seismicity does not show such a clear structure. Remarkable is also that the epicentres do not fit well to the plate boundary in the Bird (2003) plate model but are offset by about 50 to 100 km to the North. The plate boundary identified by Bird (2003) changes in this

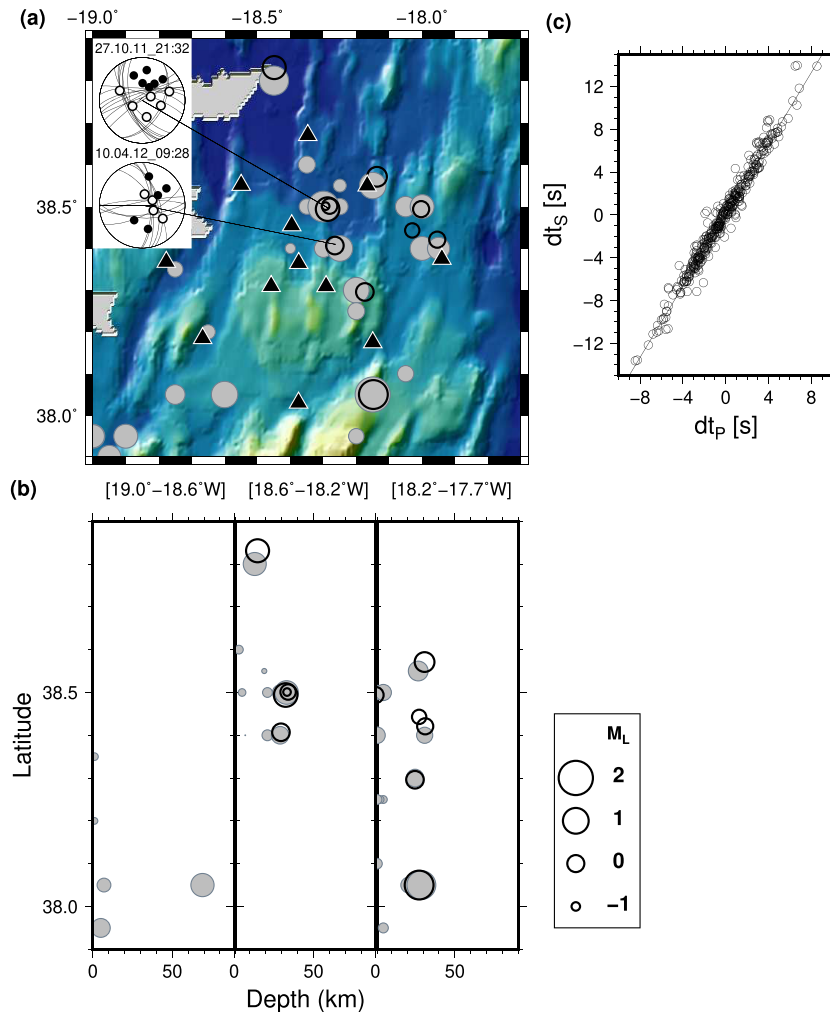


Figure 14. (a) Event epicentres localized beneath and around OBS array with the backprojection method (filled grey circles) and epicentres located using traveltime picks (open black circles) plotted on high resolution bathymetry (EMEP, Task group for the Extension of the Continental Shelf). Black triangles mark the position of the OBS array stations. Insert shows focal mechanism plots for two events within the deep ocean array constrained by P-wave polarities in lower hemisphere projection. Compressional P-wave motion is marked by black circles, extensional motion by white circles. (b) Hypocentres plotted in 0.43° wide bins in longitude as function of depth and latitude. (c) Difference between S-wave arrival times versus difference in P-wave arrival times from manual traveltime picks. The black line corresponds to a regression fit with slope 1.664 ± 0.014 .

region the strike angle and follows an obvious fault expression in the bathymetry. In general, magnetic anomaly maps also clearly image the Gloria Fault structure, however, they do not provide any indication for structures in the study region (Luis & Miranda 2008) which correlate with the observed seismicity. Integrating both, bathymetric and seismicity information, we speculate that the northward offset of the seismicity with respect to the bathymetric expression of the Gloria fault may be caused by a widening of the fault zone in two or more branches forming a left stepping restraining bent with dextral kinematics leading to a local compressive regime and the formation of thrust faults and folds. Alternatively, the northern branch indicated by seismicity may have been activated by the 1941 event.

The OBS array and Madeira array observations confirm the previously observed intraplate seismicity in the oceanic lithosphere between the OBS array position and the Iberian peninsula and Northwest Africa in the East both north and south of the plate boundary. About 12 events are located near the hypocentre of the 26 May 1975 $M_w = 7.9$ earthquake (Kaabouben *et al.* 2008, see Figs 1 and 12).

Of special interest is the seismicity near and west of Madeira. Madeira was hit by earthquakes several times in the past, where the most severe damage was caused by an earthquake near the capital of Funchal on 31 March 1748 (Chambers 1755). The seismic catalogue shows an earthquake cluster near to the island to the South at about 32.5°N , 16.5°W , a few earthquakes to the West at larger distance around 33°N , 19.5°W and a large cluster of seismicity around the epicentre of the 26 May 1975 $M 7.9$ earthquake. Only one event with $M_L = 4.5$ on 6 December 2012 is located further west at 34.07°N , 20.62°W . We locate with the OBS array about twenty events in the vicinity and west of Madeira. Seven out of the twenty events can be observed at the Madeira array stations, partially due to high noise at many Madeira array stations during daytime. The open black thick line circles in Fig. 12 show locations obtained in addition to the OBS array backazimuths and *Po/So* traveltimes with the *Po/So* traveltimes at the stations of the Madeira array. Some of the epicentres shift up to 70 km, mainly in northern direction. Our results indicate that there might be an active structure at about 33.5°N , 20.0°W in addition to the activity at about 33°N , 19.5°W .

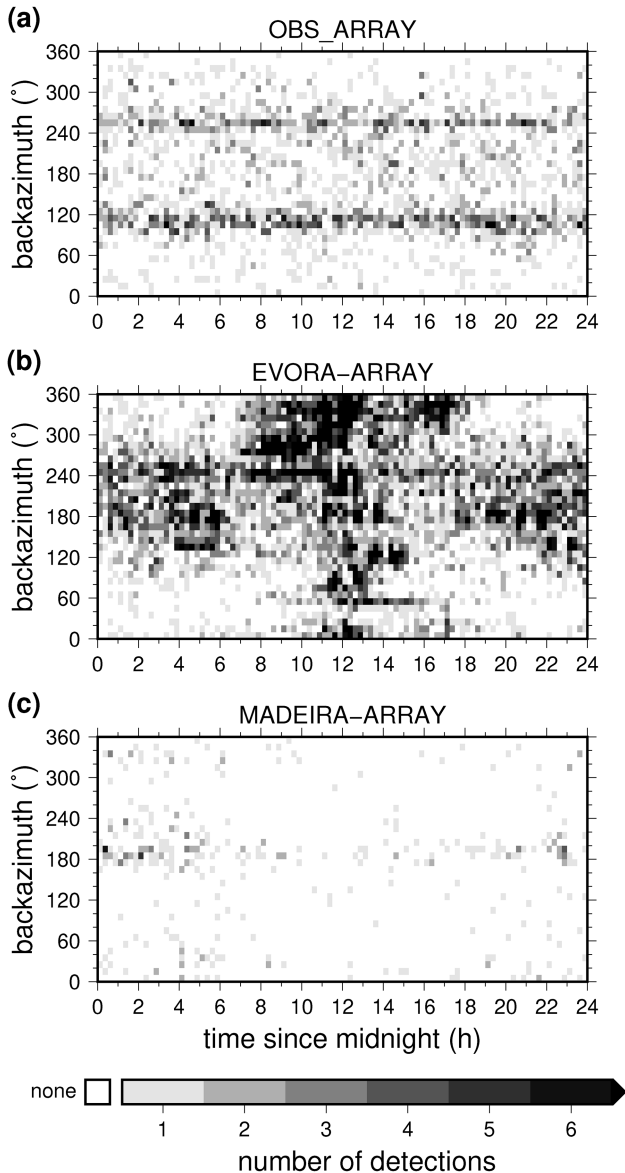


Figure 15. Backazimuths for all arrivals detected at the respective array as function of time after midnight of the respective day.

In the east it is remarkable that only a few stronger events on the continent and shelf area can be observed at the OBS array, while many events which occurred in the oceanic lithosphere between the OBS array and the Strait of Gibraltar are detected. We suspect that the differences in the continental and oceanic lithosphere and the fact that the earthquakes on the continent and shelf occur in the upper crust are the factors which are responsible for the small amplitudes of *Po/So* wave trains. However, we can also not exclude a purely distance dependent effect, insofar all events on the shelf and on the Iberian peninsula were below magnitude $M_L = 4.2$ in the observation period of the OBS array.

6.4 Seismicity beneath the OBS array

We found several earthquakes up to magnitude $M_L = 1.3$ beneath the OBS array or its immediate surroundings. Hypocentre locations determined with a backprojection/source-scanning algorithm scheme agree well with hypocentre locations based on manual picks

for selected events (Fig. 14). No clear seismic active structure in the sense of a fault trace is obvious in Fig. 14. More interesting are the revealed hypocentre depths. Within the aperture of the OBS array, where hypocentre depth determination is most accurate, we find no event below 30 km depth, but clusters between 20 and 30 km depth and shallow events. It has to be mentioned that we used for location the local CRUST1.1 velocity model (see Table 2). If the PREM model is used without a sediment layer on top, the hypocentre depths only change by 1–3 km. Table 2 also shows the average v_p/v_s velocity model obtained from polarization analysis of teleseismic *P* waves (Hannemann *et al.* 2016). This differs from the local CRUST1.1 model mainly by a higher upper mantle velocity ($v_s = 5.05 \pm 0.4 \text{ km s}^{-1}$ versus $v_s = 4.51 \text{ km s}^{-1}$) and a thicker sediment column (0.8 km versus 0.1 km). For vertical incidence *S* wave traveltimes only differ by 3 per cent for an assumed hypocentre depth of 25 km. Using the velocity model published in Batista *et al.* (2017) (northern part of the profile on the European Plate) for the location of the events beneath DOCTAR results in an hypocentre depth decrease by about 3 km for events located in the centre of the array. Unusual is the low v_p/v_s ratio of 1.664 measured for local events (see Fig. 13 and next paragraph) which is much lower than the v_p/v_s ratio of 1.85 in the local CRUST1.1 model or the v_p/v_s ratios in the range of 1.73–1.9 given in Batista *et al.* (2017). Given the same average *P*-wave velocity, hypocentres would shift to larger depths (i.e. from 30 km to about 38 km), if a depth estimate is calculated with the higher v_s .

The depth of seismicity is often attributed to the depth of the 600 °C isotherm (Abercrombie & Ekström 2001; Liu *et al.* 2012) which in turn is related to the elastic thickness of the oceanic lithosphere (Watts & Zhong 2000). Our observed hypocentre depths follow closely the elastic thickness values for fracture zones as given in Watts & Zhong (2000) for oceanic lithosphere with an age of about 70 Ma. They are larger than the seismogenic thickness found for transform faults by Abercrombie & Ekström (2001) by modelling teleseismic waveforms. Even larger hypocentre depths are found to the South of the OBS array closer to the Gloria fault with hypocentres up to 70 km depth. However, as mentioned above, uncertainties in the hypocentre depth determination increase with increasing distance to the OBS array and therefore such large hypocentre depths may be overestimated.

For two events we could constrain the focal mechanism from *P*-wave polarity readings. Two more events likely show similar polarity patterns. The events are of strike-slip character with one steep nodal plane in east–west orientation more or less in parallel to the strike of the Gloria fault. We did not try to use *S*-wave polarities or *P* to *S* amplitude ratios because the *S*-waveforms are strongly influenced by the low velocity sediment layer beneath the OBS stations.

7 CONCLUSIONS

Using incoherent beamforming and backprojection we demonstrated that recordings of the large aperture deep sea seismological DOCTAR array located in the eastern Northeast Atlantic ocean can be used to monitor the seismicity in the near- and far-regional oceanic lithosphere better than similar arrays placed near the continental margin in western Portugal and on Madeira Island west of Northwest Africa. The observed wave onsets correspond to *Po* and *So* wave trains travelling with apparent velocities similar to *P*- and *S*-wave velocities of the upper mantle lid. We located in the observation period of 10 months 355 events in the magnitude

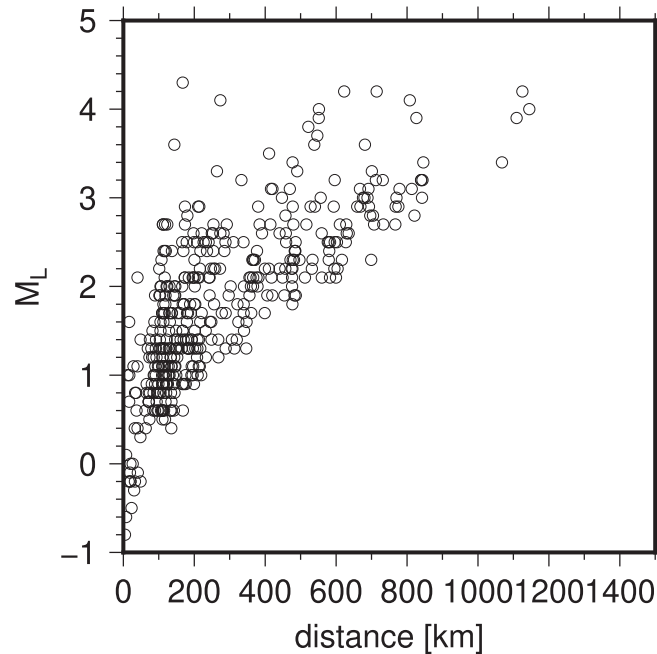


Figure 16. M_L magnitudes for all located events as function of distance to DOCTAR array station D01.

range $-0.5 \leq M_L \leq 5.2$ with epicentral distances to the array central station D01 ranging from about 5 km to about 1100 km. The events concentrate near the plate boundary between the oceanic parts of the Eurasian Plate in the North and the African Plate in the South. Earthquake clusters are detected within the oceanic plates north and south of the Gloria fault indicating active intraplate structures. Events beneath the Azores plateau and west of it are not observed as are events in the east near the continental margins. We also located earthquakes directly south of the array near the location of the 25 November 1941 M_w 8.1 event where a gap in the small magnitude event locations might indicate the lateral rupture extent. We located 16 small magnitude earthquakes directly beneath the DOCTAR array in hypocentre depths up to 30 km. Two focal mechanisms support local strike-slip tectonics. We conclude that sparsely distributed seismic arrays in the deep ocean could decrease the detection and location threshold for events in the oceanic plate and might constitute a valuable tool to monitor oceanic plate seismicity.

ACKNOWLEDGEMENTS

We have used open source software and would like to gratefully acknowledge: GIMP; Inkscape; GMT - The Generic Mapping Tools developed by Paul Wessel and Walter H.F. Smith G69; Seismic Handler (seismic waveform analysis tool) developed by Dr Klaus Stammler and Dr Marcus Walther G65, and ObsPy (Beyreuther *et al.* 2010). The authors thank EMEPC (Task Group for the Extension of the Continental Shelf) for providing the bathymetric data and Luis Batista for sharing them. We greatly acknowledge the DEPAS instrument pool for allocation of the OBS stations, the University of Hamburg for allocating ship time, and the great help of the Poseidon crew during deployment and recovery of the OBS stations (RV Poseidon cruises POS416 and POS431). We want to acknowledge the helpful comments of the scientific editor Martin Schimmel, two anonymous reviewers and the associate editor.

REFERENCES

- Abercrombie, R.E. & Ekström, G., 2001. Earthquake slip on oceanic transform faults, *Nature*, **410**, 74–77.
- Argus, D.F., Gordon, R.G. & DeMets, C., 2011. Geologically current motion of 56 plates relative to the no-net-rotation reference frame, *Geochem. Geophys. Geosyst.*, **12**, doi:10.1029/2011GC003751.
- Alfred-Wegener-Institut Helmholtz-Zentrum für Polar- und Meeresforschung *et al.*, 2017. DEPAS (Deutscher Geräte-Pool für amphibische Seismologie): German Instrument Pool for Amphibian Seismology, *J. Large-scale Res. Facilit.*, **3**, A122, doi:10.17815/jlsrf-3-165.
- Baptista, M.A., Miranda, J.M., Batllo, J., Lisboa, F., Luis, J. & Macia, R., 2016. New study on the 1941 Gloria fault earthquake and tsunami, *Nat. Hazards Earth Syst. Sci.*, **16**, 1967–1977.
- Batista, L., Hübscher, C., Terrinha, P., Matias, L., Afilhado, A. & Lüdman, T., 2017. Crustal structure of the Eurasia-Africa plate boundary across the Gloria fault, North Atlantic Ocean, *Geophys. J. Int.*, **209**, 713–729.
- Beyreuther, M., Barsch, R., Krischer, L., Megies, T., Behr, Y. & Wassermann, J., 2010. ObsPy: a Python toolbox for seismology, *Seismol. Res. Lett.*, **81**(3), 530–533.
- Bird, P., 2003. An updated digital model of plate boundaries, *Geochem. Geophys. Geosyst.*, **4**(3), doi:10.1029/2001GC000252.
- Borges, J.F., Fitas, A.J. S., Bezzeghoud, M. & Teves-Costa, P., 2001. Seismotectonics of Portugal and its adjacent Atlantic area, *Tectonophysics*, **337**, 373–387.
- Bufo, E., Udias, A. & Colombas, M.A., 1988. Seismicity, source mechanisms, and tectonics of the Azores–Gibraltar plate boundary, *Tectonophysics*, **152**, 89–118.
- Carrilho, F., Nunes, J.C., Pena, J. & Senos, M.L., 2004. *Catálogo Sísmico de Portugal Continental e Região Adjacente Para o Período 1970–2000*, p. 227. Inst. Meteorol. Lisboa.
- Carrilho, F. & Vales, D., 2009. Calibration of magnitude M_L for Portugal and adjacent areas, in *6 Simposio de Meteorologia e Geofísica da APMG*, pp. 48–53, Assoc. Port. De Meteorol. E Geofis.
- Chambers, C., 1755. Account of the earthquake at Madeira, *Phil. Trans. Abr.* **x.**, 665.
- Custodio, S., Lima, V., Vales, D., Cesca, S. & Carrilho, F., 2016. Imaging active faulting in a region of distributed deformation from the joint clustering of focal mechanisms and hypocentres: Application to the Azores–western Mediterranean region, *Tectonophysics*, **676**, 70–89.

- DeMets, C., Gordon, R.G. & Argus, D.F., 2010. Geologically current plate motions, *Geophys. J. Int.*, **181**, 1–80.
- Dziewonski, A.M. & Anderson, D.L., 1981. Preliminary reference Earth model, *Phys. Earth planet. Inter.*, **25**(4), 297–356.
- Ekström, G., Nettles, M. & Dziewonski, A.M., 2012. The global CMT project 2004–2010: centroid-moment tensors for 13,017 earthquakes, *Phys. Earth planet. Inter.*, **200/201**, 1–9.
- Fernandes, R.M.S., Ambrosius, B.A.C. & Noomen, R., 2003. The relative motion between Africa and Eurasia as derived from ITRF2000 and GPS data, *Geophys. Res. Lett.*, **30**(16), doi:10.1029/2003GL017089.
- Geldmacher, J., Bogaard, P.V.D., Hoernle, K.A. & Schmincke, H.U., 2000. The ⁴⁰Ar/³⁹Ar age dating of the Madeira Archipelago and hotspot track (eastern North Atlantic), *Geochem. Geophys. Geosyst.*, **1**, doi:10.1029/1999GC000018.
- Geldmacher, J., Hoernle, K., Bogaard, P.V.D., Duggen, S. & Werner, R., 2005. New ⁴⁰Ar/³⁹Ar age and geochemical data from seamounts in the Canary and Madeira volcanic provinces: support for the mantle plume hypothesis, *Earth planet. Sci. Lett.*, **237**, 85–101.
- Gente, P., Dymant, J., Maia, M. & Goslin, J., 2003. Interaction between the Mid-Atlantic-Ridge and the Azores hot spot during the last 85 Myr: emplacement and rifting of the hot spot-derived plateaus, *Geochem. Geophys. Geosyst.*, **4**(10), doi:10.1029/2003GC000527.
- Gibbons, S.J., Ringdal, F. & Kvaerna, T., 2008. Detection and characterization of seismic phases using continuous spectral estimation on incoherent and partially coherent array, *Geophys. J. Int.*, **172**, 405–421.
- Grigoli, F., Cesca, S., Vassallo, M. & Dahm, T., 2013. Automated seismic event location by travel-time stacking: an application to mining induced seismicity, *Seismol. Res. Lett.*, **84**, 666–677.
- Gutenberg, G. & Richter, C.F., 1949. *Seismicity of the Earth and Associated Phenomena*, 273pp, Princeton Univ. Press.
- Hannemann, K., Krüger, F. & Dahm, T., 2014. Measuring of clock drift rates and static time offsets of ocean bottom stations by means of ambient noise, *Geophys. J. Int.*, **196**(2), 1034–1042.
- Hannemann, K., Krüger, F., Dahm, T. & Lange, D., 2016. Oceanic lithospheric S wave velocities from the analysis of P wave polarization at the ocean floor, *Geophys. J. Int.*, **207**, doi:10.1093/gji/ggw342.
- Hannemann, K., Krüger, F., Dahm, T. & Lange, D., 2017. Structure of the oceanic crust and upper mantle north of the Gloria Fault in the eastern mid Atlantic by receiver function analysis, *J. geophys. Res.*, **122**(10), 7927–7950.
- Hart, R.S. & Press, F., 1973. S_n velocities and the composition of the lithosphere in the regionalized Atlantic, *J. geophys. Res.*, **78**(2), 407–411.
- Hensen, C. *et al.*, 2019. Marine transform faults and fracture zones: a joint perspective integrating seismicity, fluid flow and life, *Front. Earth Sci.*, **7**, 39, doi:10.3389/feart.2019.00039.
- Hoernle, K., Zhang, Y.S. & Graham, D., 1995. Seismic and geochemical evidence of large scale mantle upwelling beneath the eastern Atlantic and western and central Europe, *Nature*, **374**, 34–39.
- Bormann, P. & Dewey, J.W., 2013. The new IASPEI standards for determining magnitudes from digital data and their relation to classical magnitudes, Information sheet IS 3.3, in *New Manual of Seismological Observatory Practice 2 (NMSOP2)*, pp. 1–33, ed. Bormann, P., Potsdam: Deutsches GeoForschungsZentrum GFZ, doi:10.2312/GFZ.NMSOP-2-ch3.
- International Seismological Centre, 2015. *On-line Bulletin*, <http://www.isc.ac.uk>, Internatl. Seismol. Cent., Thatcham, United Kingdom.
- Kaabouben, F., Brahim, A.I., Toto, E., Baptista, M.A., Miranda, J.M., Soares, P. & Luis, J.F., 2008. On the focal mechanism of the 26.05.1975 North Atlantic event: contribution from tsunami modeling, *J. Seismol.*, **12**, 575–583.
- Kao, H. & Shan, S.-J., 2004. The source-scanning algorithm: mapping the distribution of seismic sources in time and space, *Geophys. J. Int.*, **157**, 589–594.
- Kennett, B.L.N. & Furumura, T., 2013. High-frequency Po/So guided waves in the oceanic lithosphere: I—long distance propagation, *Geophys. J. Int.*, **195**, 1862–1877.
- Kennett, B.L.N. & Furumura, T., 2015. Toward the reconciliation of seismological and petrological perspectives on oceanic lithosphere heterogeneity, *Geochem. Geophys. Geosyst.*, **16**, 3129–3141.
- Klügel, A., Schwarz, S., Bogaard, P., Hoernle, K.A., Wohlgemuth-Ueberwasser, C.C. & Köster, J.J., 2009. Structure and evolution of the volcanic rift zone at Ponta de São Lourenço, eastern Madeira, *Bull. Volcanol.*, **71**, 671–685.
- Linehan, D., 1940. Earthquakes in the West Indian region, *EOS, Trans. Am. geophys. Un.*, **21**, 229–232.
- Laske, G., Masters, G., Ma, Z. & Pasyanos, M.E., 2013. CRUST1.0: an updated global model of Earth's crust, in *EGU General Assembly 2012*, held 22–27 April, 2012 in Vienna, Austria, p.3743. Abstract EGU2013-2658.
- Lewis, J.F. & Mirande, J.M., 2008. Reevaluation of magnetic chrons in the North Atlantic between 35°N and 47°N: implications for the formation of the Azores Triple Junction and associated plateau, *J. geophys. Res.*, **113**, B101105, doi:10.1029/2007JB005573.
- Liu, Y., McGuire, J.J. & Behn, M.D., 2012. Frictional behavior of oceanic transform faults and its influence on earthquake characteristics, *J. geophys. Res.*, **117**(1), doi:10.1029/2011JB009025.
- Lynnes, C.S. & Ruff, L.J., 1985. Source process and tectonic implications of the great 1975 North Atlantic earthquake, *Geophys. J. Int.*, **82**, 497–510.
- Madeira, J., Brum da Silveira, A., Hipolito, A. & Carmo, R., 2015. Chapter 3 active tectonics in the central and eastern Azores islands along the Eurasia–Nubia boundary: a review, *Geol. Soc. Lond. Mem.*, **44**, 15–32.
- Mallik, S. & Frazer, L.N., 1990. Po/So synthetics for a variety of oceanic models and their implications for the structure of the oceanic lithosphere, *Geophys. J. Int.*, **100**, 235–253.
- Mata, J., Kerich, R., MacRae, N.D. & Wu, C.Y., 1998. Elemental and isotopic (Sr, Nd and Pb) characteristics of Madeira island basalts: evidence for composite HIMU EM I plume fertilizing lithosphere, *Can. J. Earth Sci.*, **35**, 980–997, doi:10.1139/e98-046.
- Matos, C., Silveira, G., Matias, L., Caldeira, R., Ribeiro, M.L., Nuno, A.D., Krüger, F. & dos Santos, T.B., 2015. Upper crustal structure of Madeira Island revealed from ambient noise tomography, *J. Volc. Geotherm. Res.*, **298**, 136–145.
- Matos, C., Custódio, S., Batlló, J., Zahradník, J., Arroucau, P. & Silveira, G., 2018. An active seismic zone in intraplate west Iberia inferred from high resolution geophysical data, *J. geophys. Res.*, **123**(4), 2885–2907.
- Müller, R.D., Sdrolias, M., Gaina, C. & Roest, W.R., 2008. Age, spreading rates, and spreading asymmetry of the world's ocean crust, *Geochem. Geophys. Geosyst.*, **9**(4), doi:10.1029/2007GC001743.
- Neidell, N.S. & Taner, M.T., 1971. Semblance and other coherency measures for multichannel data, *Geophysics*, **36**, 482–497.
- NOAA World Data Service for Geophysics, 1969. *Marine Seismic Reflection Survey ID V2707*, available at: <https://www.ngdc.noaa.gov/mgg/seismicreflection/index.html>, last accessed 25 February 2016.
- Pilidou, S., Priestley, K., Gudmundsson, O. & Debayle, E., 2004. Upper mantle S-wave speed heterogeneity and anisotropy beneath the North Atlantic from regional surface wave tomography: the Iceland and Azores plumes, *Geophys. J. Int.*, **159**, 1057–1076.
- Rost, S. & Thomas, C., 2002. Array seismology, *Rev. Geophys.*, **40**(3), 1–27.
- Schweitzer, J., 2001. HYPOSAT—an enhanced routine to locate seismic events, *Pure appl. Geophys.*, **158**, 277–289.
- Schweitzer, J., Fyen, J., Mykkeltveit, S., Gibbons, S.J., Pirl, M., Kuehn, D. & Kvaerna, T., 2012. Seismic arrays, in *New Manual of Seismological Observatory Practice (NMSOP-2)*, ed. Bormann, P., GFZ German Research Centre for Geosciences (Deutsches GeoForschungsZentrum GFZ). ISBN 3-9808780-0-7.9.: 1–80.
- Bonnefoy-Claudet, S. *et al.*, 2005. Report on FK/SPAC Capabilities and limitations, WP06, Derivation of dispersion curves, European Commission – Research General Directorate Project No. EVG1-CT-2000-00026 SESAME.

- Serpelloni, E., Vannucci, G., Pondrelli, S., Argnani, A., Casula, G., Anzidei, M., Baldi, P. & Gasperini, P., 2007. Kinematics of the Western Africa-Eurasia plate boundary from focal mechanisms and GPS data, *Geophys. J. Int.*, **169**, 1180–1200.
- Shito, A., Suetsugu, D., Furumura, T., Sugioka, H. & Ito, A., 2013. Small-scale heterogeneities in the oceanic lithosphere inferred from guided waves, *Geophys. Res. Lett.*, **40**, 1708–1712, doi:10.1002/grl.50330 .
- Silveira, G., Stutzmann, E., Davaille, A., Montagner, J.P., Mendez-Victor, L. & Sebai, A., 2006. Azores hotspot signature in the upper mantle, *J. Volc. Geotherm. Res.*, **126**, 23–34.
- Silveira, G., Vinnik, L., Stutzmann, E., Farra, V., Kiselev, S. & Morias, I., 2010. Stratification of the Earth beneath the Azores from P and S receiver functions, *Earth planet. Sci. Lett.*, **299**, 91–103.
- Snoke, J.A., Munsey, J.W., Teague, A.C. & Bollinger, G.A., 1984. A program for focal mechanism determination by combined use of polarity and SV-P amplitude ratio data, *Earthq. Notes*, **55**(3), 15.
- Stähler, S.C. *et al.*, 2016. Preliminary performance report of the RHUM-RUM ocean bottom seismometer network around La Réunion, western Indian Ocean, *Adv. Geosci.*, **41**, 43–63.
- Stammler, K., 1993. Seismichandler-Programmable multichannel data handler for interactive and automatic processing of seismological analyses, *Comp. Geosci.*, **19**(2), 135–140.
- Udias, A., Lopez Arroyo, A. & Mezcua, J., 1976. Seismotectonics of the Azores–Alboran region, *Tectonophysics*, **31**, 259–289.
- Walker, D.A. & Sutton, G.H., 1971. Oceanic mantle phases recorded on hydrofones in the North Western Pacific at distances between 9 and 40 degree, *Bull. seism. Soc. Am.*, **61**, 65–78.
- Watts, A.B. & Zhong, S., 2000. Observations of flexure and the rheology of oceanic lithosphere, *Geophys. J. Int.*, **142**, 855–875.
- Wessel, P., Smith, W.H.F., Scharroo, R., Luis, J. & Wobbe, F., 2013. Generic mapping tools: improved version released, *EOS, Trans. Am. geophys. Un.*, **94**(45), 409–410.